Physics of the Dark Universe 50 (2025) 102151

Contents lists available at ScienceDirect

Physics of the Dark Universe

journal homepage: www.elsevier.com/locate/dark

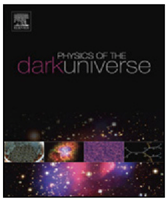

Full length article

Accretion disk luminosity and topological characteristics for a Schwarzschild black hole surrounded by a Hernquist dark matter halo

Luis M. Nieto [a,*], Farokhnaz Hosseinifar [b], Kuantay Boshkayev [c,d], Soroush Zare [a,b,e], Hassan Hassanabadi [a,d,f]

[a] Departamento de Física Teórica, Atómica y Optica and Laboratory for Disruptive, Interdisciplinary Science (LaDIS), Universidad de Valladolid, 47011 Valladolid, Spain
[b] Center for Theoretical Physics, Khazar University, 41 Mehseti Street, Baku, AZ-1096, Azerbaijan
[c] National Nanotechnology Laboratory of Open Type, 050040 Almaty, Kazakhstan
[d] Al-Farabi Kazakh National University, Al-Farabi ave. 71, 050040 Almaty, Kazakhstan
[e] Helsinki Institute of Physics, University of Helsinki, P.O. Box 64, FI-00014, Helsinki, Finland
[f] Department of Physics, Faculty of Science, University of Hradec Králové, Rokitanského 62, 500 03 Hradec Králové, Czechia

ARTICLE INFO

Keywords:
Black hole
Dark matter
Accretion disk
Luminosity
Topological characteristics

ABSTRACT

In this work, we analyze some characteristics and gravitational signatures of the Schwarzschild black hole immersed in a Hernquist dark matter halo. We determine the black hole's remnant radius and mass, which provide useful residual information at the end of its evaporation, and we then explore the luminosity of the accretion disk for the model under study. In this way, we determine the key orbital parameters of the test particles within the accretion disk, such as angular velocity, angular momentum, energy, and the radius of the innermost stable circular orbit, based on the dark matter model parameters. We also numerically estimate the accretion disk's efficiency in converting matter into radiation. We also demonstrate that dark matter, which significantly alters the geometry surrounding a Schwarzschild black hole, influences the accretion disk's radiative flux, temperature, differential luminosity, and spectral luminosity. The stability of a black hole spacetime is determined in the eikonal regime. The Lyapunov exponent is also analyzed to quantify the stability of the particle regime and to demonstrate the infall into or escape from the black hole to infinity, as well as the quasi-normal modes. Finally, some properties of black holes are studied from a topological perspective.

1. Introduction

In recent years, experimental studies in gravitational physics have made considerable progress, providing compelling evidence for the existence of extraordinary astrophysical objects such as black holes [1,2,2–5]. In particular, the LIGO/Virgo, Event Horizon Telescope (EHT), and GRAVITY collaborations have achieved groundbreaking discoveries through their coordinated efforts. These include the detection of gravitational wave signals resulting from binary black hole mergers [6,7], observations of the event horizon shadow of the supermassive black holes M87* and Sgr A* within the core of the galaxy M87 [8,9] and Sgr A* [10], and the detection of infrared flares near our galactic center [11]. The study of black holes (BH) is used to understand the dynamics of galaxies and how they influence their evolution [12–17]. Black holes exhibit extremely strong gravitational phenomena and high-energy physics, such as quasiperiodic oscillations, the formation of gigantic particle jets, gravitational lenses, and the disruption of nearby stars. From a theoretical point of view, BHs are like a laboratory in which one can test different predictions made by the theories of modified gravity, quantum gravity, and other small- or large-distance corrections to general relativity [1].

In parallel with the study of BH, dark matter has emerged as a cornerstone of modern cosmology, accounting for a large percentage of the total mass–energy content of the universe [18,19]. The concept of dark matter was first introduced in the early 20th century [20,21]. In 1933, while studying the Coma galaxy cluster, Zwicky observed that the visible mass of the galaxies was insufficient to explain the observed gravitational binding, leading him to propose the existence of an additional invisible mass that would provide the gravitational attraction necessary to hold the cluster together [22]. At the end of the 20th century, this idea gained more attention [23–25]. For example, the rotation curves of spiral galaxies indicated that stars in

---

* Corresponding author.

E-mail addresses: luismiguel.nieto.calzada@uva.es (L.M. Nieto), f.hoseinifar94@gmail.com (F. Hosseinifar), kuantay@mail.ru (K. Boshkayev), szare@uva.es (S. Zare), hha1349@gmail.com (H. Hassanabadi).

https://doi.org/10.1016/j.dark.2025.102151
Received 18 August 2025; Received in revised form 9 October 2025; Accepted 24 October 2025

the outer regions were moving much faster than expected based on visible mass alone [26,27]. Based on cosmological models, the total mass–energy content of the universe is estimated to be composed of 5% ordinary or baryonic matter, about 27% dark matter, and about 68% dark energy [28–30]. The different models in the exploration of dark matter share the common idea that dark matter has mass and contributes to gravity, it does not emit, absorb or reflect light and there are cases in which it has no electromagnetic interactions, although it does interact gravitationally and can affect galaxies, gravitational lenses and cosmic structure [31,32]. Since this type of matter does not interact with electromagnetic forces, it is invisible and its existence is inferred through gravitational effects on visible matter [20,33,34]. According to some models, dark matter behaves like a perfect fluid and can be considered a collisionless fluid, and due to its stability, it has a long lifetime. Dark matter can be classified as cold, warm, or hot, depending on whether the respective masses are of the order sub- eV, KeV, or GeV [35–37]. This findings led to further investigations into the nature of dark matter. In [38], an analytical expression for the radius of the BH's shadow was found, assuming a simple spherical configuration of dark matter around it, and their estimates show that dark matter is unlikely to manifest itself in the shadows of galactic BH, unless its concentration near the BH is anomalously high. The importance of dark matter goes far beyond its gravitational influence [39–42], and so, for example, it plays a crucial role in the formation and evolution of cosmic structures, guiding the assembly of galaxies and clusters from primordial density fluctuations imprinted during the inflationary phase of the early Universe [43–46]. Current cosmological models, particularly the cold dark matter framework, claim that dark matter halos form hierarchically through the merging of smaller structures over time and are made of elementary particles that were not relativistic at early times [47–50].

Dark matter halos provide the gravitational framework within which baryonic matter can cool and condense, ultimately forming stars and galaxies. The dynamics of objects within galaxies are significantly affected by dark matter halos. The structural properties of these haloes, including their density profiles and mass distributions, are characterized using various mathematical models [32,51,52]. Several density profiles are frequently employed to describe dark matter halos, each one representing the characteristics of different galaxies. The Hernquist profile is significant for its effectiveness in describing the internal structure of dark matter halos, characterized by a central peak and a pronounced decrease in density at larger radii [53–56]. This profile facilitates the modeling of the gravitational potentials and the understanding of the dynamics of stars within galaxies. Recent advances in N-body simulations have provided deeper insights into the assembly and evolution of dark matter halos, revealing how their structures influence galaxy formation and the cosmos in general [57]. Axial quasinormal modes (QNM) of black holes immersed in Hernquist-type dark matter halos have been investigated, revealing a universal relationship between the matter environment and redshift QNMs [58]. The distribution of Hernquist-type matter near supermassive BH has been investigated, focusing on how this distribution affects key orbital properties, such as innermost stable circular orbits (ISCOs), as a function of the surrounding dark matter environment [59]. Polar perturbations of BH surrounded by the Hernquist profile and their influence on gravitational wave generation and energy fluxes in extreme mass-ratio spirals [60] have also been examined.

The investigation of accretion disks surrounding compact objects is a possible way to discern the distinctions between general relativity and several alternative theories of gravity [61–72], as well as the astrophysical environments in which BH are found [73–78]. Accretion refers to the gravitational infall of matter onto a compact object, such as a BH, resulting in the redistribution of energy and the generation of high-energy astrophysical phenomena, including relativistic jets and quasars [79–83]. Accretion disks are optically thick and geometrically thin structures that form as infalling gas conserves angular momentum. They initially follow metastable orbits before transitioning to unstable trajectories influenced by the geometry of the spacetime [84]. In this way, gravitational energy transforms into thermal radiation through viscous dissipation and magnetohydrodynamic interactions, with emissions reaching their peak in the inner regions of the disk, where relativistic effects prevail. The velocity distribution of accreting matter and the curvature of spacetime are the determining factors of the radiation spectrum, which spans wavelengths from radio to X-rays. Fundamental geodesic structures, such as photon orbits and the ISCO, define the limits of stable motion in the vicinity of a BH. In geometrically thin accretion disks, the ISCO determines the inner radius of the disk, beyond which matter immediately falls into the event horizon. The boundary is crucial in determining the observable characteristics of the BH and the accretion efficiency. Perturbations caused by pressure variations, magnetic fields, or relativistic frame dragging give rise to epicyclic oscillations with distinct radial and vertical components. In the innermost regions of the accretion disk, these oscillations manifest as the quasi-periodic variability observed in BH systems and leave a characteristic imprint on the emitted spectrum. Understanding orbital motion and epicyclic frequency is essential for investigating the relativistic accretion dynamics and spacetime geometry of BH. Extensive research has been carried out on BH accretion disks [85–104], attracting significant attention in the scientific literature.

In this work, we propose to investigate BH surrounded by a Hernquist-type dark matter distribution. This model offers a more realistic representation of the matter environment around BH, unlike simpler assumptions such as the Schwarzschild or Kerr solutions. The paper is organized as follows. In Section 2, by exploring the thermodynamic properties of these BH at the event horizon, we seek to contribute new insights into the structure of BH spacetime in the presence of dark matter. We present a brief review of the spacetime model of the BH surrounded by a Hernquist-type dark matter distribution and determine the thermodynamic properties at the horizon. In Section 3, we review the geodesic motion of massive particles traveling through the corresponding static and spherically symmetric spacetime. Subsequently, we explore the parameters of the geometrically thin accretion disk, inspired by the Novikov–Thorne and Page–Thorne models, and apply them to the SBH–HDM solution. Furthermore, the study of geodetic motion in these spacetimes provides crucial information about the trajectories of test particles and accretion processes, both key to understanding the physics of accretion disks. Our exploration of the geometrically thin accretion disk, within the framework of the SBH–HDM solution, provides an updated perspective on the formation and evolution of these disks, with implications for observational signatures such as radiation profiles. In Section 4 we evaluate the impact of the mass density (MD) on the QNMs in the eikonal regime and in Section 5 we study topological thermodynamics. Finally, in Section 6 we summarize the main results of this article and draw our conclusions. The metric signature adopted in this study is $(- + ++)$, with the constants set as $G = \hbar = c = 1$.

2. Thermodynamic properties

The spacetime metric of pure dark matter can be determined by considering the relationship between the tangential velocity (in the equatorial plane) and the static and spherically symmetric spacetime metric coefficients. Subsequently, by considering the dark matter halo within a general static spherically symmetric spacetime as an extension of the energy–momentum tensors in the Einstein field equation, solutions for spherically symmetric BH with a dark matter halo will be derived. In this section, we summarize the main equations characterizing a static, spherically symmetric BH spacetime surrounded by a region with a Hernquist density profile. For further technical details on the derivation of the spacetime geometry for the SBH–HDM model, which has been used to study the thermodynamic and optical properties of a Schwarzschild BH immersed in a Hernquist-type dark matter distribution (SBH–HDM) [53], we refer the reader to [105]. Therefore, the SBH–HDM metric is expressed as

$$ds^2 = -f(r)dt^2 + \frac{dr^2}{g(r)} + h(r)(d\theta^2 + \sin^2\theta d\phi^2). \tag{1}$$

The density profile of the Hernquist dark matter halo is given by [106]

$$\rho(r) = \rho_s \left(\frac{r}{r_s}\right)^{-1}\left(1 + \frac{r}{r_s}\right)^{-3}, \tag{2}$$

where ρ_s refers to the characteristic density and r_s denotes the scale radius of the dark matter halo. Fig. 1 shows the variation of the Hernquist halo density profile for $\rho_s = 1$ and three r_s cases.

The mass profile of the dark matter distribution is

$$M_{DM}(r) = \int_0^r 4\pi\rho(r')r'^2 dr' = \frac{2\pi\rho_s r^2 r_s^3}{(r + r_s)^2}. \tag{3}$$

Using the tangential velocity of the particle $v_t^2 = M_{DM}/r$, considering $g(r) = f(r)$ in Eq. (1), and applying Einstein's field equations $R_{\mu\nu} - \frac{1}{2}Rg_{\mu\nu} = \kappa^2(T^H_{\mu\nu} + T^B_{\mu\nu})$, where $T^H_{\mu\nu}$ and $T^B_{\mu\nu}$ represents the energy–momentum tensor for dark matter halo (H) and Schwarzschild black hole (B), respectively (both obtained from $T^\nu_\mu = g^{\nu\lambda}T_{\mu\lambda} = \mathrm{diag}\left[\rho, p_r, p, p\right]$), R refers to Ricci scalar, $R_{\mu\nu}$ indicates Ricci tensor, and $g_{\mu\nu}$ is the metric tensor of the line element (1), the author of Ref. [105] performed a detailed calculation and derived the explicit forms of the functions $f(r)$ and $h(r)$ appearing in (1), which are given by

$$f(r) = 1 - \frac{2M}{r} - \frac{4\pi\rho_s r_s^3}{r + r_s}, \qquad h(r) = r^2, \tag{4}$$

where it can be observed that the lapse function $f(r)$ behaves asymptotically flat in $r \to \infty$. Fig. 2 shows the shape of $f(r)$ for three cases of r_s.

At the horizon the lapse function is zero, therefore the horizon radius is obtained as

$$r_\pm = \frac{1}{2}\left(2M - r_s + 4\pi\rho_s r_s^3 \pm \sqrt{8Mr_s + \left(r_s - 2M - 4\pi\rho_s r_s^3\right)^2}\right). \tag{5}$$

In the limit of $r_s \to 0$, $r_+ \to 2M$ and $r_- \to 0$, and so it turns out that r_+ tends to the Schwarzschild BH horizon. Therefore, the radius of the BH event horizon in the presence of Hernquist dark matter is considered $r_h = r_+$.

The mass of the BH as a function of horizon radius is obtained from $f(r_h) = 0$ and is

$$M(r_h) = r_h\left(\frac{1}{2} - \frac{2\pi\rho_s r_s^3}{r_h + r_s}\right), \tag{6}$$

which approaches the mass of the Schwarzschild BH in the limit of $r_s \to 0$ or $\rho_s \to 0$.

The Hawking temperature is calculated from $1/(4\pi)\,\partial_r f(r)\big|_{r=r_h}$ and by substituting the mass given in Eq. (6), the following result is obtained [107–109]

$$T_H = \frac{1}{4\pi r_h} - \frac{\rho_s r_s^4}{r_h(r_h + r_s)^2}, \tag{7}$$

where it is evident that in the limit of $r_s \to 0$ or $\rho_s \to 0$, Eq. (7) tends to the Hawking temperature of the Schwarzschild BH. Fig. 3 illustrates the behavior of the Hawking temperature in terms of the horizon radius for three values of r_s.

The remnant radius of the BH, which indicates the radius after the evaporation process, is calculated from $T_H\big|_{r=r_{\mathrm{rem}}} = 0$ and reads [110–112]

$$r_{\mathrm{rem}} = r_s\left(2r_s\sqrt{\pi\rho_s} - 1\right). \tag{8}$$

It can be concluded that maintaining the condition $2\sqrt{\pi\rho_s}r_s > 1$, the remnant radius is positive. This parameter is important because if it is different from zero, at the end of the evaporation process the information will not disappear. Fig. 4 illustrates the variation of the remnant radius in terms of r_s for three values of ρ_s. As expected from Eq. (8) and obvious in Fig. 4, increasing r_s and ρ_s results in an increase in the remnant radius. If the horizon radius in the BH mass Eq. (6) is substituted by the remnant radius from Eq. (8), the remnant mass of the BH can be obtained.

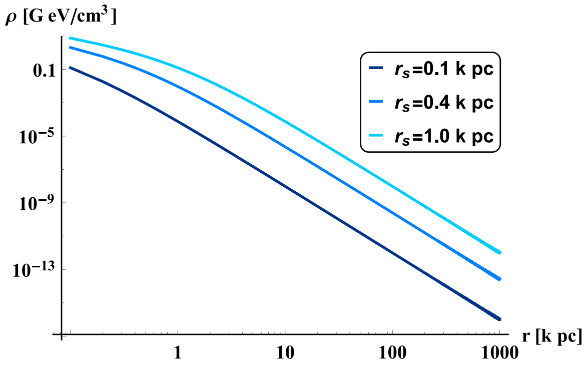

Fig. 1. Density profile in terms of r considering $\rho_s = 1\,\mathrm{GeV/cm^3}$ for three values of r_s. Increasing r_s results in an increase in density for each constant r.

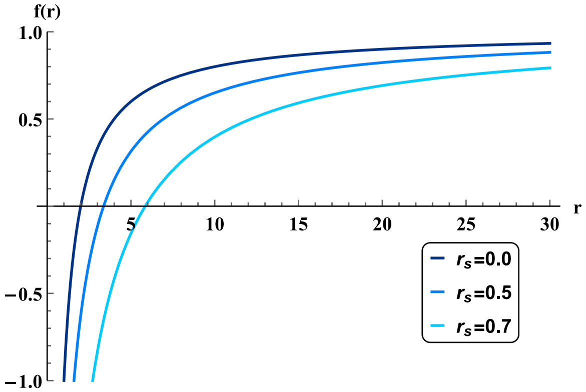

Fig. 2. Lapse function for $\rho_s = 1$ and three values of r_s in terms of r. This function is asymptotically flat and tends to 1 as r increases. The case $r_s = 0$ represents the Schwarzschild BH function, and as the influence of the parameter r_s increases, the size of the horizon also increases.

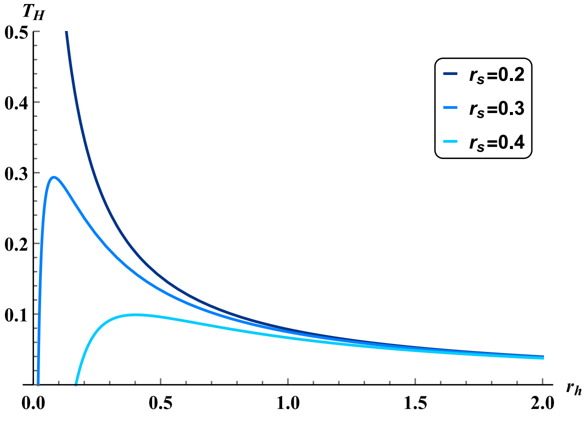

Fig. 3. Hawking temperature curves for $\rho_s = 1$ and three values of r_s versus the horizon radius. An increase in the parameter r_s causes the Hawking temperature to reach a maximum, resulting in a phase transition when r_s is chosen above a certain threshold. Furthermore, increasing the size of r_s causes this phase transition to occur at a larger radius.

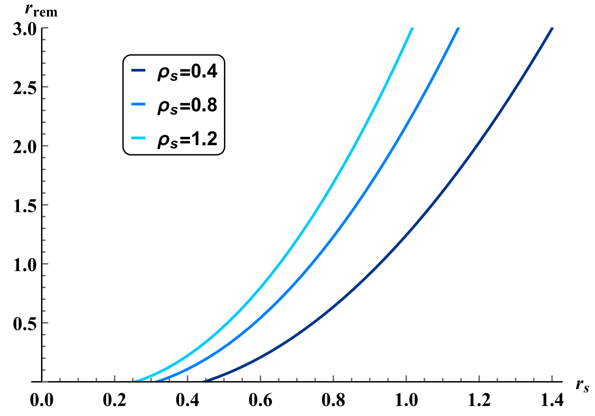

Fig. 4. Remnant radius of the BH versus r_s for three different values of ρ_s. For a remnant radius to exist, a specific condition must be met in the selection of the parameters r and ρ_s. If this is true, an increase in the size of either of these parameters results in an increase in the remnant radius.

3. Radiative flux and spectral luminosity of the accretion disk

We begin this section with a brief review of the physical characteristics of thin accretion disks according to the Novikov–Thorne model [80], which is a more general version of the Shakura–Sonyaev model [79]. The model is based on some conventional assumptions: (I) the spacetime of the central massive entity is stationary, axisymmetric, and asymptotically flat; (II) the disk mass has no influence on the background metric; (III) the accretion disk is assumed to be geometrically thin, with its vertical scale height essentially negligible compared to its radial extent; (IV) the orbiting particles are confined between the outer radius r_{OUT} and the innermost stable circular orbit r_{ISCO}, which defines the inner boundary of the disk; (V) the accretion disk is confined to the equatorial plane ($\theta = \pi/2$) of the central compact object, so that its surface lies perpendicular to the BH's spin axis; (VI) under the assumption of hydrodynamic and thermodynamic equilibrium, the disk emits electromagnetic radiation with a blackbody spectrum characteristic of its local temperature; (VII) the mass accretion rate, $\dot{m}$, is considered constant in time [100]. The radiation emanating from the accretion disk can be strongly affected by the parameters of the BH, making this research essential for understanding the physical characteristics of BH and their effects on the results of astrophysical observations. In this work, we first investigate the ISCO of massive test particles within the BH's gravitational field, described by the spacetime metric (1). Next, we explore the radiative properties of the disk, which are essential for characterizing its observable signatures. To do this, it is first necessary to explore the geometry of the space where particles travel near a compact object [88]. The Lagrangian governing the geodesic motion of test particles moving around a massive object is [113–115]:

$$2\mathcal{L} = g_{\mu\nu}\dot{x}^{\mu}\dot{x}^{\nu} = -f(r)\dot{t}^2 + \frac{\dot{r}^2}{f(r)} + h(r)(\dot{\theta}^2 + \sin^2\theta\dot{\phi}^2), \tag{9}$$

where the dot represents the derivative with respect to τ, which is an affine parameter along the geodesic $x^{\mu}(\tau)$. The metric coefficients are only functions of the radial coordinate r. Furthermore, we employ an equatorial approximation, indicating that $|\theta - \pi/2| \ll 1$. Since the aforementioned metric does not depend on the coordinates t and ϕ, we expect to have two constants of motion, namely the energy E and the angular momentum per unit rest-mass L [116–118], given by

$$E = f(r)\dot{t}, \qquad L = h(r)\dot{\phi}, \tag{10}$$

A significant attribute of the thin accretion disk is the effective potential $V_{\mathrm{eff}}(r)$. The radial equation of motion is derived from the relation $\mathcal{L} = -1/2$, considering Eqs. (9) and (10), as follows:

$$\frac{1}{2}\dot{r}^2 + V_{\mathrm{eff}}(r) = \frac{1}{2}E^2, \tag{11}$$

in which the effective potential is

$$V_{\mathrm{eff}}(r) = \frac{f(r)}{2}\left(1 + \frac{L^2}{r^2}\right). \tag{12}$$

The circular orbit moves through the minimum point of the effective potential. In the absence of a minimum (i.e., when the potential exhibits“smooth” behavior), circular orbits are unstable at a specific point. The ISCO is related to a marginally stable circular orbit. For such a trajectory, the conditions $\frac{dr}{d\tau} = 0$ and $\frac{d^2r}{d\tau^2} = 0$ must be met. To ensure marginal stability, the additional requirement $d^3r/d\tau^3 = 0$ must also be met. Applying these requirements to Eq. (11), the following equivalent set of expressions is obtained [104,119]:

$$V_{\mathrm{eff}}(r) = \frac{1}{2}E^2, \qquad \partial_r V_{\mathrm{eff}}(r) = 0, \qquad \text{and} \qquad \partial_r^2 V_{\mathrm{eff}}(r) = 0. \tag{13}$$

All circular orbits beyond the ISCO are stable, unless there is an outermost stable circular orbit. Only the first two equations of (13) are required for general circular orbits. These equations can be used to obtain both the specific energy E and angular momentum L of a massive particle in a circular orbit of radius r [120]:

$$\begin{aligned} L(r) &= \frac{\Omega(r)h(r)}{\sqrt{f(r) + \Omega(r)^2 h(r)}} \\ &= \frac{r\sqrt{M(r+r_s)^2 + 2\pi\rho_s r^2 r_s^3}}{\sqrt{r\left((r+r_s)^2 - 2\pi\rho_s r_s^3(3r+2r_s)\right) - 3M(r+r_s)^2}}, \end{aligned} \tag{14}$$

$$\begin{aligned} E(r) &= \frac{f(r)}{\sqrt{f(r) + \Omega(r)^2 h(r)}} \\ &= \frac{(r-2M)(r+r_s) - 4\pi\rho_s r r_s^3}{\sqrt{r\left((r-3M)(r+r_s)^2 - 2\pi\rho_s r r_s^3(3r+2r_s)\right)}}. \end{aligned} \tag{15}$$

The angular velocity of the particle in the orbit is given by [121]

$$\Omega(r) = \sqrt{\frac{\partial_r f(r)}{\partial_r h(r)}} = \frac{\sqrt{M(r+r_s)^2 + 2\pi\rho_s r^2 r_s^3}}{r^{3/2}(r+r_s)}, \tag{16}$$

where Eqs. (14), (15) and (10) have been used [80,120]. The requirement $\partial_r^2 V_{\mathrm{eff}}(r) = 0$ gives r_{ISCO}. Hence, the radius of the ISCO surrounding the SBH–HDM can be determined by [122]

$$E(r)^2\partial_r^2 h(r) - L(r)^2\partial_r^2 f(r) - \partial_r^2(f(r)h(r))\Big|_{r=r_{\mathrm{ISCO}}} = 0. \tag{17}$$

Using $f(r)$ and $h(r)$ from Eq. (4), and angular velocity, energy, and angular momentum from Eqs. (14)–(16), and substituting them into Eq. (17), r_{ISCO} is calculated from Eq. (18) in Box I. A dark matter halo surrounding a BH modifies the gravitational field felt by nearby particles, which can cause the ISCO to shift outward if the halo exerts a strong pull. The magnitude of this shift depends on characteristics of the halo, such as its density and slope, and most models suggest the ISCO radius increases compared to empty space solutions. Because the ISCO is sensitive to these changes, it can help scientists study the area around BHs, allowing them to gather observational data on X-ray emissions from surrounding accretion disks [123–125]. Fig. 5 illustrates the variation of the ISCO radius as a function of r_s/M, together with the angular velocity, angular momentum, and energy profiles for $\rho_s M^2 = 1$ and selected values of r_s/M, plotted as functions of the radial coordinate r/M. As expected, in the limit of $r_s \to 0$, the BH metric function in Eq. (4) tends to that of the Schwarzschild BH. Consequently, the initial value of the black hole's ISCO radius is similar to the Schwarzschild black hole's ISCO radius, which is $6M$. With a constant r_s/M and an increase in $\rho_s M^2$, the total mass increases, resulting in greater stability as the particle is positioned at a larger radius. An increase in either the r_s/M or $\rho_s M^2$ parameters leads to an increase in the size of the ISCO radius. For small r_s/M, the sensitivity of r_{ISCO} to variations in $\rho_s M^2$ is low. However, as r_s/M increases, the sensitivity of r_{ISCO} to changes in $\rho_s M^2$ becomes more pronounced. On the other hand, at constant $\rho_s M^2$, the sensitivity of $\Omega(r)$ to changes

$$\frac{2M(6M-r)(r+r_s)^3-4\pi\rho_s r r_s^3\left(r^2(r+3r_s)-2M\left(6r^2+9rr_s+r_s^2\right)\right)+48\pi^2\rho_s^2 r^3 r_s^6}{r(r+r_s)\left((r-3M)(r+r_s)^2-2\pi\rho_s r r_s^3(3r+2r_s)\right)}\Bigg|_{r_{\rm ISCO}}=0. \tag{18}$$

Box I.

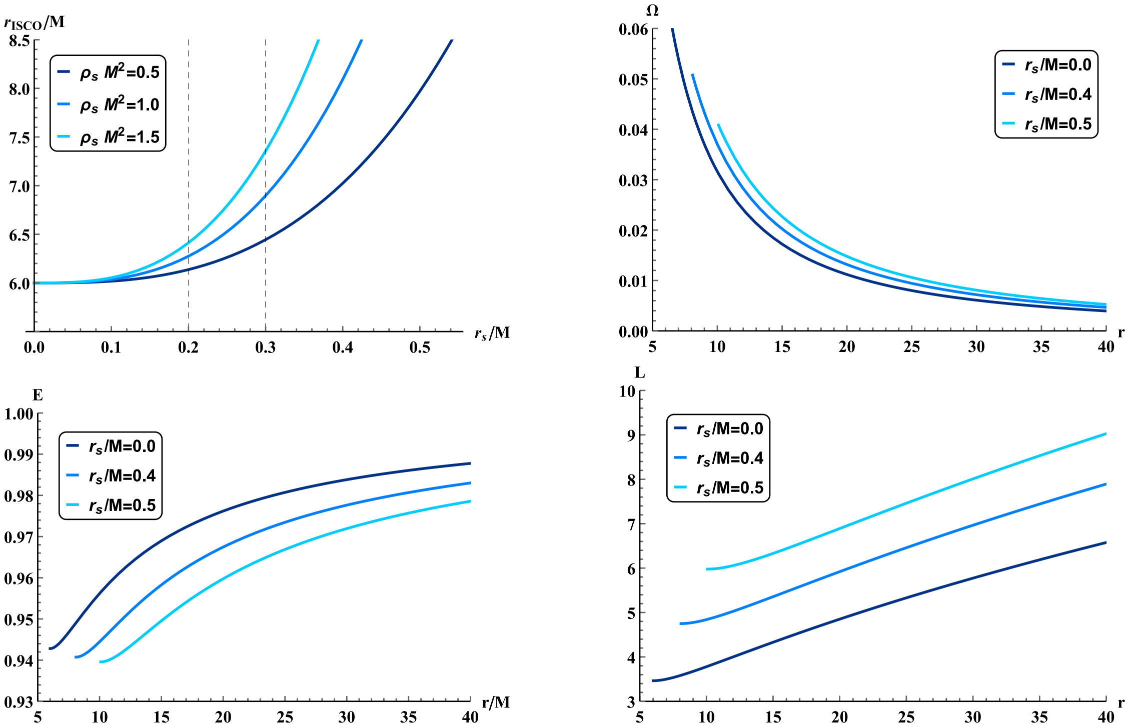

Fig. 5. The radius of the ISCO, $r_{\rm ISCO}$, in terms of r_s/M, and the behavior of angular velocity, angular momentum, and energy considering $\rho_s M^2 = 1$. The presence of the Hernquist dark matter around the BH, although it increases the ISCO radius and raises the value of $\Omega(r)$ and $E(r)$, decreases the magnitude of the angular momentum of the test particle.

in r_s/M is low, while the sensitivities of $L(r)$ and $E(r)$ are higher. In the presence of Hernquist dark matter, particles on the accretion disk exhibit higher values of velocity and angular momentum, as well as lower energy compared to the Schwarzschild BH. As r_s/M increases, the disparity in these quantities for the Hernquist dark matter BH compared to the Schwarzschild BH becomes more pronounced. In all cases, as r/M approaches infinity, we expect Ω to tend toward zero, as the effects of dark matter diminish. Furthermore, with r/M constant, increasing r_s/M results in a larger angular velocity due to the increased mass. The angular velocity decreases with increasing orbital radius, and with dark matter the angular velocity is slightly greater at the same radius because the presence of dark matter adds additional mass content outside the BH and thus orbiting particles feel a stronger pull and must move faster to maintain circular motion and the Hernquist halo causes the angular velocity at a given radius to be greater than the Schwarzschild, as the halo adds gravitational mass. Of course, angular velocity always decreases as the radius increases because gravity is weaker further away.

In relativistic orbital mechanics, the specific energy $E(r)$ is the conserved energy per unit rest mass of a test particle, and we expect that at infinity, the energy reaches saturation $E = 1$ that means just the rest energy and for bound orbits, $E < 1$. Therefore, it is obvious that the smaller $E(r)$, the stronger the particle's binding. Comparing Schwarzschild dark matter with Schwarzschild + Hernquist dark matter (SBH–HDM), Fig. 5 shows that, for the same radius, $E(r)$ in the halo case is slightly smaller than in Schwarzschild, meaning that the particles in the halo case are more bound.

On the other hand, $L(r)$ is larger in the presence of dark matter than in the Schwarzschild with the same radius. With the presence of dark matter, the gravitational attraction becomes stronger than in the Schwarzschild case, and to maintain equilibrium against the greater gravitational attraction (BH + halo), the particles must have greater orbital angular momentum, and in this case, the centrifugal barrier is stronger. If we consider a particle orbiting the BH, with just the BH, it needs a certain angular momentum to keep it from falling inward, but with additional mass including the BH plus dark matter, it must spin faster (higher L) to keep it from falling inward.

The energy flux emitted by the accretion disk surrounding the BH refers to the amount of energy radiated per unit area per unit time, and is measured at the ISCO. It is obtained from [126–128]

$$\mathcal{F}(r)=-\frac{\dot{m}}{4\pi\sqrt{h(r)}}\frac{\partial_r\Omega(r)}{(E(r)-\Omega(r)L(r))^2}\int_{r_{\rm ISCO}}^{r}(E(R)-\Omega(R)L(R))\partial_R L(R)dR, \tag{19}$$

where $\dot{m}$ is the accretion rate mass. Since all the physical quantities under the integral are well defined, we do not face any problem related to numerical integration, since explicit analytical expressions even exist for them. The integration is performed from $r_{\rm ISCO}$ to an arbitrary distance. For simplicity, we can assume it is constant and take $\dot{m} = 1$, which is equivalent to taking into account the normalized flux per

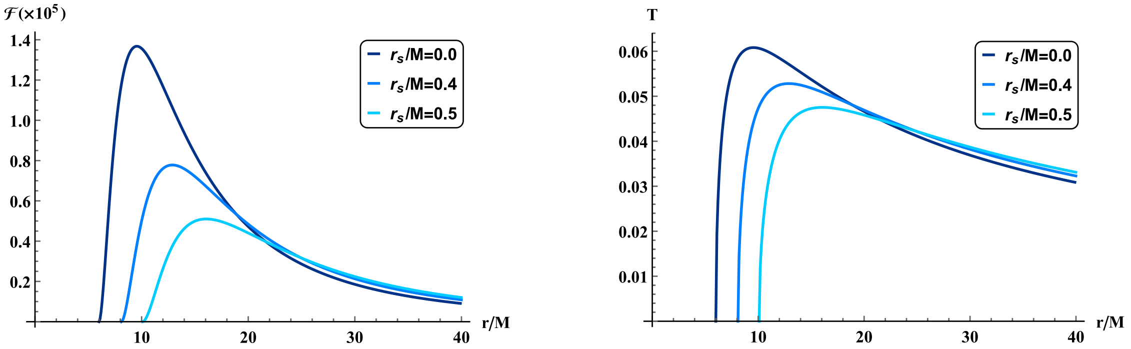

Fig. 6. For $\rho_s M^2 = 1$, the energy flux is represented in the left panel and the radiation temperature in the right panel. Although the presence of Hernquist dark matter increases the energy flux and radiation temperature at small r/M, at large r/M this effect is reversed and the presence of Hernquist dark matter decreases the energy flux and radiation temperature.

unit accretion rate, i.e., $\mathcal{F}(r)/\dot{m}$ [120]. Using the Stefan–Boltzmann law, $\mathcal{F}(r) = \sigma_{SB} T(r)^4$, where $T(r)$ refers to the radiation temperature and σ_{SB} indicates the Stefan–Boltzmann constant.

Fig. 6 shows the energy flux and radiation temperature curves considering $\rho_s M^2 = 1$ for three different values of r_s/M.

The regions closest to the BH are hotter and brighter, but due to the Hernquist dark matter distribution from zero to infinity, the gravitational pull extends outward. The innermost region of the disk cools slightly, while the outer regions radiate more intensely than in the pure Schwarzschild case. Inside the ISCO, matter plunges into the BH in unstable orbits. Once it passes through, it can no longer maintain a circular trajectory and falls almost freely. Due to its rapid fall, there is no time for viscous stresses to extract orbital energy and convert it into radiation. The peak flux/temperature is not at the innermost point because, inside the ISCO, matter is falling too quickly to radiate, and this is where maximum dissipation occurs. Hence, maximum radiation occurs just outside the ISCO, where viscous processes are still active. In the case of the Hernquist halo, the shape of the gravitational potential changes, shifting the location where viscous stresses can operate most efficiently. As a result, the flux/temperature peak shifts outward, and the maximum value is somewhat reduced compared to the Schwarzschild. It is observed that as r/M increases, the energy flux reaches a maximum value before subsequently decreasing, and as r_s/M increases, the maximum value of $\mathcal{F}(r)$, which is located at $\partial_r \mathcal{F}(r)\big|_{r=r_c} = 0$, also decreases, occurring at a smaller r/M value. Although the energy flux for the Schwarzschild BH is initially higher at small radii compared to the BH with Hernquist dark matter, the magnitude of energy flux increases in the presence of Hernquist dark matter at larger radii. The larger the r_s/M, the greater the value of $\mathcal{F}$. A similar trend is observed for the radiation temperature.

Figs. 7–8 depict the behavior of the radiation temperature density. In Fig. 7, considering $\rho_s M^2 = 1$, the radiation temperature variations are graphed on an x–y Cartesian plane corresponding to the equator. After crossing the horizon (marked by the black disk), the emitted temperature is initially zero, reaches its maximum after the ISCO radius, and then gradually decreases. As anticipated in Fig. 6, while increasing the parameter r_s/M leads to a reduction in the maximum source radiation temperature, this maximum occurs at a larger radius. Furthermore, while at smaller radii, a lower r_s/M corresponds to higher temperatures, at larger radii, a higher r_s/M results in higher temperature values.

Fig. 8 shows the temperature behavior in terms of r/M and r_s/M. As indicated in Fig. 6, as r_s/M increases, the maximum radiation temperature decreases and occurs at a larger radius.

By fixing $\dot{m}$, the differential luminosity at infinity, which indicates the total amount of energy emitted by the accretion disk per unit time that reaches an observer at infinity, is determined as [93,129,130]

$$\frac{d\mathcal{L}_\infty}{d\ln r} = 4\pi r^2 E(r)\mathcal{F}(r). \tag{20}$$

The spectral luminosity distribution at spatial infinity is calculated from [131,132]

$$\nu\mathcal{L}_{\nu,\infty} = \frac{15}{\pi^4}\int_{r_i}^{\infty}\left(\frac{d\mathcal{L}_\infty}{d\ln r}\right)\frac{(u(r)y)^4}{M_T^2\mathcal{F}(r)}\,\frac{1}{\exp\left(\dfrac{u(r)y}{\left[M_T^2\mathcal{F}(r)\right]^{1/4}}\right)-1}\,d\ln r, \tag{21}$$

where

$$u(r) = \frac{1}{\sqrt{f(r) + \Omega^2(r)h(r)}}. \tag{22}$$

Here M_T is the total mass of the BH and the halo, with the halo mass given in Eq. (3), and the variable y is $y = \hbar\nu/kT_*$, where $\hbar$ is Plank's constant, ν is the radiation frequency, k indicates the Boltzmann constant and $T_* = \dot{m}/\left(4\pi M_T^2 \sigma_{\rm SB}\right)$.

Fig. 9 represents the variation of the differential luminosity at infinity and the spectral luminosity for $\rho_s M^2 = 1$ and three values of r_s/M. Different accretion disk radii emit at different frequencies. Dark matter re-tunes the spectrum, since at small radii the halo-enhanced BH disk emits less total light (lower peak), and at larger radii, the halo disks radiate more intensely, redistributing the spectrum. Schwarzschild is bluer-hot, but HDM disks are slightly redder and broader, and the spectral peak is shifted. Hernquist dark matter reshapes the observable spectrum, which is a crucial astrophysical signature that can help distinguish BHs in dense DM environments. It is observed that the differential luminosity at infinity exhibits energy flux-like behavior, and at constant $\rho_s M^2$, an increase in r_s/M results in a lower maximum value of $\frac{d\mathcal{L}_\infty}{d\ln r}$, which occurs at lower r/M.

The right panel of Fig. 9 illustrates how the presence of a Hernquist dark matter halo modifies the spectral luminosity of the accretion disk compared to the standard Schwarzschild case. In the Schwarzschild geometry, the innermost regions of the disk remain hotter, resulting in a larger contribution at high frequencies, especially in the blue and X-ray bands of the spectrum. Conversely, when the BH is embedded in a dark matter halo, the gravitational influence of the halo redistributes the dissipation of orbital energy over a wider region of the disk. This redistribution results in a cooler inner disk and a comparatively brighter outer disk. The spectral energy distribution shifts toward lower frequencies: the luminosity increases in the low-energy regime (red, optical, and infrared) but is suppressed at higher energies (blue and X-ray). In general, this behavior reflects the fact that dark matter halos broaden the spatial extent of efficient radiation while reducing the maximum temperature of the accretion disk, thus producing a redder and less intense spectrum in the high-frequency tail than that of a naked Schwarzschild BH. It is evident that while at small r/M the spectral luminosity of the BH in the presence of Hernquist dark matter is higher and increases with higher r_s/M, at a large r/M the trend is reversed and the Schwarzschild BH exhibits a higher luminosity.

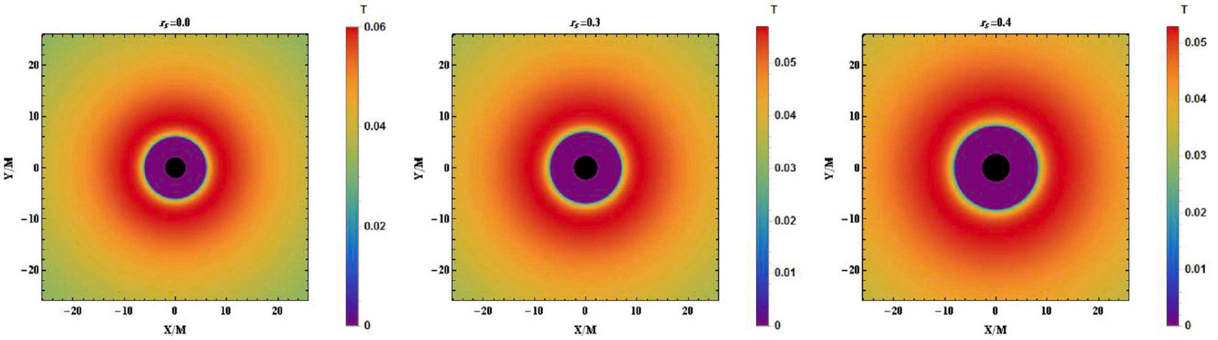

Fig. 7. Radiation temperature for $\rho_s M^2 = 1$ in the equatorial Cartesian coordinate plane $x - y$.

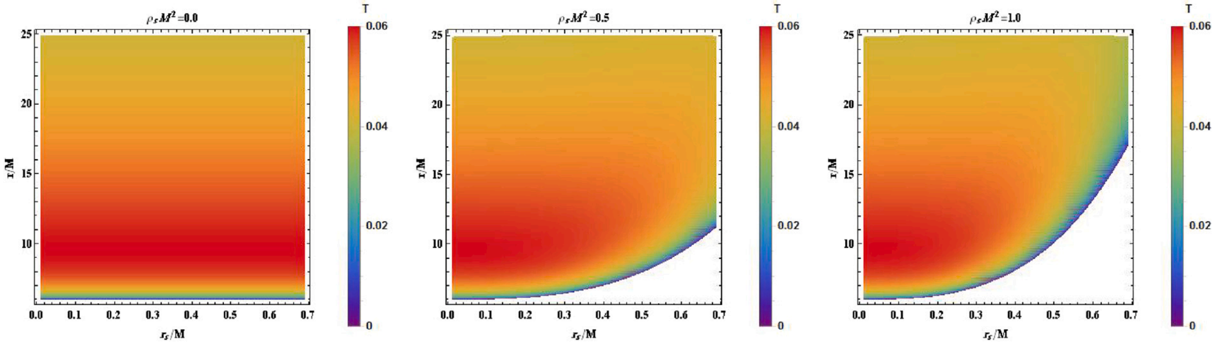

Fig. 8. The behavior of the radiation temperature when varying r_s/M and r/M for three options of $\rho_s M^2$.

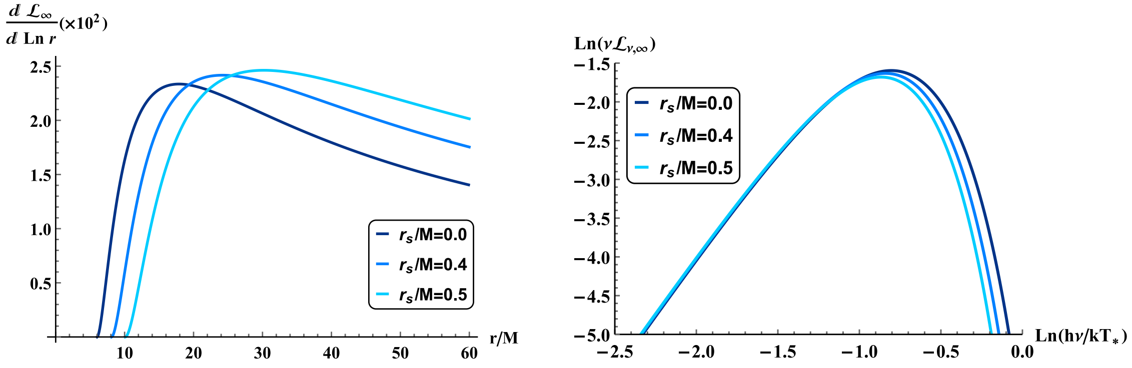

Fig. 9. For $\rho_s M^2 = 1$, the differential luminosity at infinity is shown in the left panel and the observed spectral luminosity in the right panel.

Redshift is the change in frequency (or wavelength) of a photon, measured by different observers, resulting from two main effects: gravitational redshift, where photons lose energy as they scape from a gravitational field, and Doppler shift, where relative motion alters the frequency. Together, these effects reveal information about both the motion of the source and observer and the gravitational field the photon has passed through [133,134]. The ratio between the frequency of a photon detected by a distant observer and the emitted frequency, as influenced by the redshift, is calculated from [125]

$$\tilde{g}(r) = \frac{1}{1+z} = \frac{\sqrt{f(r) - r^2 \sin^2\theta\,\Omega^2(r)}}{1 + \Omega(r) r \sin\phi \sin\tilde{\psi}}, \tag{23}$$

where $\tilde{\psi}$ refers to small inclination angle that we set to $\tilde{\psi} = 0$, and $f(r)$ and $\Omega(r)$ are defined in (4) and (16), respectively. In Table 1, we present the redshift-factor for some values of r_s/M and $\rho_s M^2$ at the first, second, and third multiples of $r_{\rm ISCO}/M$. In Fig. 10, the curve of $\tilde{g}$ as a function of r/M is presented considering $\rho_s M^2 = 1$ for the case $\theta = \pi/6$. We note that, for flat spacetime, as r/M approaches infinity, redshift factor converges to unity and becomes independent of the dark matter parameters. However, at smaller values of r/M, with r/M constant, increasing the parameter r_s/M decreases the magnitude of the redshift factor.

Table 1
$\tilde{g}$–factor considering $\theta = \pi/6$.

r_s/M	$\rho_s M^2$	$r_{\rm ISCO}/M$	$g(r_{\rm ISCO}/M)$	$g(2\,r_{\rm ISCO}/M)$	$g(3\,r_{\rm ISCO}/M)$
0.3	0.5	6.4445	0.7891	0.9006	0.9348
0.5	0.5	7.9705	0.7836	0.8974	0.9326
0.3	1.0	6.8970	0.7880	0.8999	0.9344
0.5	1.0	10.0894	0.6608	0.8448	0.8989

We can define the relative shift in redshift factor as

$$\delta\tilde{g}(r) = \frac{\tilde{g}^{\rm SBH{-}{-}HDM}(r) - \tilde{g}^{\rm SBH}(r)}{\tilde{g}^{\rm SBH}(r)} \tag{24}$$

In Fig. 11, $\delta\tilde{g}$ is plotted as a function of r_s/M at $r = r_{isco}$. It is observed that, in all these cases δg is negative and $\tilde{g}^{\rm SBH{-}{-}HDM}(r) < \tilde{g}^{\rm SBH}(r)$, which

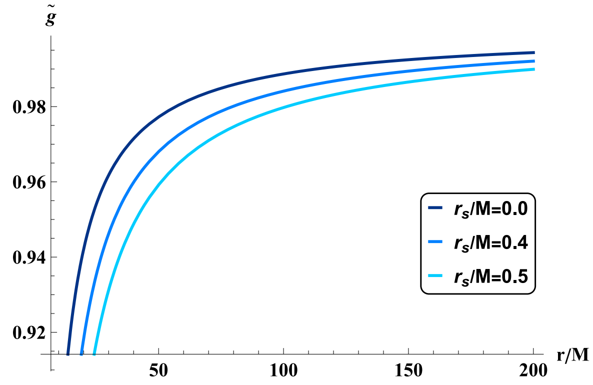

Fig. 10. Redshift factor in terms of r/M, where $\theta = \pi/6$ and $\rho_s M^2 = 1$. Although with a small r/M an increase in the parameter effect should lead to a decrease in $\tilde{g}$-factor, with a large r/M the redshift factor approaches one.

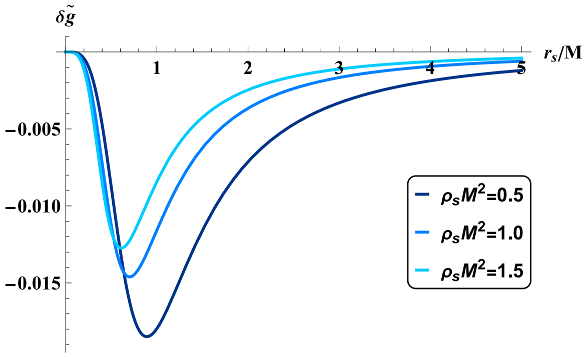

Fig. 11. Variation of $\delta\tilde{g}$ in terms of r_s/M for three $\rho_s M^2$ cases considering $\theta = \pi/6$. These curves are plotted for the ISCO radius, and considering that the $\tilde{g}$-factor of the Schwarzschild BH is larger than the $\tilde{g}$-factor of the BH in the presence of Hernquist dark matter, $\delta\tilde{g}$ has a negative value.

coincides with our expectations from Fig. 10. For all the above cases, we assume that the distant observer is at infinity.

Compared to a Schwarzschild BH in vacuum, it is also intriguing to determine the radiative efficiency of the source, which is the amount of energy from the disk's rest mass that is transformed into radiation, which is

$$\eta = \frac{\mathcal{L}_{\rm bol}}{\dot{m}} \simeq 1 - E(r_{\rm ISCO}), \tag{25}$$

where, in light from a Schwarzschild BH, one obtains the standard result $\eta \approx 5.72\%$ [120]. Here, the bolometric luminosity of the accretion disk is denoted by $\mathcal{L}_{\rm bol}$. Fig. 12 shows the variations in efficiency in the presence of Hernquist dark matter as the parameter r_s/M increases. As can be seen, at $r_s/M \to 0$, the efficiency equals that of the Schwarzschild BH, and as the quantity r_s/M increases, this improves. It is also observed that, while for a small value of r_s/M, the efficiency increases with increasing $\rho_s M^2$, as r_s/M gradually increases, the magnitude of this quantity becomes larger for smaller values of $\rho_s M^2$.

4. Quasi-normal modes

Quasi-normal modes (QNMs) correspond to damped oscillations defined by complex frequencies that encode energy dissipation and reveal key physical properties of BHs, such as mass, charge, and angular momentum. In this section, we explore scalar field perturbations in SBH–HDM spacetime and derive the corresponding effective potential governing their dynamics.

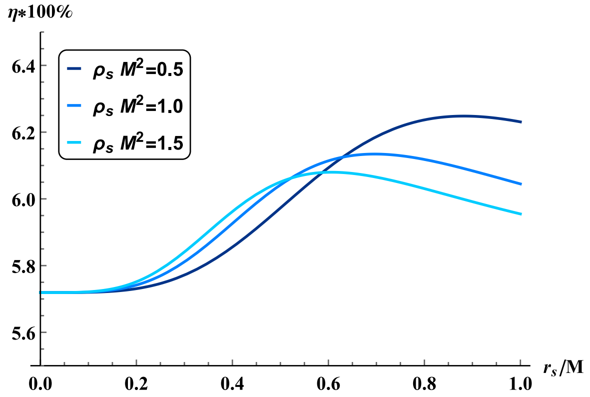

Fig. 12. Radiative efficiency in terms of r_s/M. For $r_s/M = 0$, the magnitude of the efficiency is $\eta = 5.7191\%$, which is the Schwarzschild BH efficiency.

We consider now a massless scalar field in a curved spacetime whose Klein–Gordon equation has the following form [135,136]

$$\frac{1}{\sqrt{-g}}\partial_\mu(\sqrt{-g}g^{\mu\nu}\partial_\nu \Psi_{\omega lm}(\mathbf{r},t)) = 0, \tag{26}$$

where $g_{\mu\nu}$ is the metric tensor, $-g = r^4 \sin^2\theta$ is its determinant and $g^{\mu\nu}$ is its inverse, its components being

$$g^{tt} = \frac{-1}{f(r)}, \qquad g^{rr} = f(r), \qquad g^{\theta\theta} = \frac{1}{r^2}, \qquad g^{\phi\phi} = \frac{1}{r^2\sin^2\theta} \tag{27}$$

We assume that the wavefunction is given by [137]

$$\Psi_{\omega lm}(\mathbf{r},t) = \frac{R_{\omega l}(r)}{r} Y_{lm}(\theta,\, \phi) e^{-i\omega t}, \tag{28}$$

where $Y_{lm}(\theta,\, \phi)$ is the spherical harmonics and ω is the frequency. Here, as usual, l represents the angular quantum number (multipole) and m denotes integers, provided that $l > |m|$. In the coordinates (θ,ϕ) of the 2-sphere, with $0 \le \theta < \pi$ and $0 \le \phi < 2\pi$, the Laplace–Beltrami operator for the angular part is

$$\Delta_{S^2} = \frac{1}{\sin\theta}\frac{\partial}{\partial\theta}\left(\sin\theta\frac{\partial}{\partial\theta}\right) + \frac{1}{\sin^2\theta}\frac{\partial^2}{\partial^2\phi}, \tag{29}$$

and the spherical harmonics $Y_{lm}(\theta,\phi)$ are precisely the solutions of the equation

$$\Delta_{S^2} Y_{lm}(\theta,\phi) = -l(l+1)Y_{lm}(\theta,\phi). \tag{30}$$

By inserting (27), (28) and (30) into (26) we can obtain a Schrödinger type equation:

$$\frac{d}{dr}\left(f(r)\frac{dR_{\omega l}(r)}{dr}\right) + \left(\frac{\omega^2}{f(r)} - \frac{l(l+1)}{r^2} - \frac{1}{r}\frac{df(r)}{dr}\right)R_{\omega l}(r) = 0. \tag{31}$$

Considering the tortoise coordinates as $dr^* = dr/f(r)$ [138], Eq. (31) can be written as [139]

$$\frac{d^2}{dr^{*2}}R_{\omega l}(r^*) + (\omega^2 - V_{\rm eff}(r^*))R_{\omega l}(r^*) = 0, \tag{32}$$

where $V_{\rm eff}$ refers to the Regge–Wheeler effective potential, which is used to examine the QNM of BH, and for scalar fields it is defined in Ref. [140]:

$$V_{\rm eff}(r) = f(r)\left(\frac{1}{r}\frac{df(r)}{dr} + \frac{l(l+1)}{r^2}\right). \tag{33}$$

We hypothesize that, when r_s or ρ_s are held constant, increasing the other parameter at small scales significantly alters the height of the effective potential barrier. This indicates that the presence of dark matter halos can have a substantial impact on the geometry of the spacetime surrounding Schwarzschild BH. Fig. 13 illustrates the variation of the effective potential in terms of r and r^*. As shown, increasing the parameter r_s leads to a decrease in the magnitude of the effective potential, resulting in its maximum occurring at a larger radius.

The correlation between the maximum of $V_{\rm eff}$ and the quasi-normal frequencies implies that changes in r_s or ρ_s could have comparable impacts on the quasi-normal frequencies.

Considering $Q(r^*) = \omega^2 - V_{\rm eff}(r^*)$, we obtain the following differential equation [141]

$$\frac{d^2 R_{\omega l}(r^*)}{dr^{*2}} + Q(r^*) R_{\omega l}(r^*) = 0. \tag{34}$$

In the eikonal limit, the term $\frac{f(r)}{r}\frac{\partial f(r)}{\partial r}$ is negligible, also as $l \gg 1$, so $l(l+1) \approx l^2$ and Q takes the following form

$$Q = \omega^2 - \frac{f(r)}{r^2} l^2. \tag{35}$$

Assuming that Q has a maximum at $\partial_r Q\big|_{r=r_c} = 0$, then Eq. (35) can be written as

$$Q \equiv Q(r_c) + \underbrace{\frac{1}{1!}\partial_r Q\Big|_{r=r_c}(r-r_c)}_{0} + \frac{1}{2!}\partial_r^2 Q\Big|_{r=r_c}(r-r_c)^2 + O(r^3), \tag{36}$$

where $Q(r_c) = \omega^2 - \frac{f(r_c)}{r_c^2} l^2$. The maximum of Q is calculated from $r_c \partial_r f(r)\big|_{r=r_c} - 2f(r_c) = 0$, which is similar to the circular orbit or circular null geodesic [142,143]. We therefore conclude that there exists a well-defined geometrical–optical limit, called the eikonal limit, applicable to a wide class of massless perturbations [144].

The Klein–Gordon equation considering the Taylor expansion of Q in r^* coordinates has the following eigenvalues, that are known as QNMs

$$\frac{Q(r_c)}{\sqrt{2\frac{d^2 Q(r^*)}{dr^{*2}}\Big|_{r^*=r_c}}} = i\left(n + \frac{1}{2}\right). \tag{37}$$

It should be noted that the above result is valid for asymptotically flat spacetime [144]. By substituting the value of $Q(r_c)$ from Eq. (35) into the previous equation, it reduces to

$$\omega_{\rm QNM} = l\sqrt{\left(\frac{f(r_c)}{r_c^2}\right)} - i\frac{n+\frac{1}{2}}{\sqrt{2}}\sqrt{\frac{-r_c^2}{f(r_c)}\left(\frac{d^2}{dr^{*2}}\frac{f(r^*)}{r^{*2}}\right)_{r=r_c}}. \tag{38}$$

For an asymptotically flat spacetime, the shadow is calculated from [105,116]

$$r_{sh} = \frac{r_c}{\sqrt{f(r_c)}}. \tag{39}$$

The Lyapunov exponent is a measure of how quickly light rays diverging around a photon's orbit fall into the BH or escape to infinity. For the metric of the form (1), the Lyapunov exponent is calculated from

$$|\lambda| = \frac{1}{\sqrt{2}}\sqrt{\frac{-r^2}{f(r)}\left(\frac{d^2}{dr^{*2}}\frac{f(r^*)}{r^{*2}}\right)}\Bigg|_{r=r_c}, \tag{40}$$

which determines the instability time scale of unstable null circular geodesics. Using Eq. (32), the Lyapunov exponent is obtained from

$$|\lambda| = \frac{1}{\sqrt{2}}\sqrt{\frac{-r^2}{f(r)}\left(f(r)\left(\frac{\partial}{\partial r}f(r)\frac{\partial}{\partial r} + f(r)\frac{\partial^2}{\partial r^2}\right)\frac{f(r)}{r^2}\right)}\Bigg|_{r=r_c}. \tag{41}$$

In the eikonal regime, or in the limit of geometric optics, the Lyapunov exponent of the null geodesics is related to the imaginary part of the QNM in the form

$$\omega_{\rm QNM} = \frac{1}{r_{sh}} l - i\left(n + \frac{1}{2}\right)|\lambda|. \tag{42}$$

Here, n is the overtone number. Fig. 14 illustrates the variation of the shadow and the real part of the QNM in terms of r_s, and it can be seen that an increase in r_s (ρ_s) results in an increase in the BH shadow and a reduction in the real part of the QNMs. The eikonal approximation for calculating quasinormal modes is valid under specific conditions. It applies to very high angular momentum modes, asymptotically flat spacetimes, and massless perturbations with a smooth effective potential. In particular, the effective potential must have a soft barrier with a single peak near the photon sphere.

4.1. Gray-body factors

Gray-body factors represent the modifications in the emission spectrum of BH due to the presence of potential barriers [145–147]. They consider the effects of the BH's gravitational field on the emitted radiation, its spin, and the dimensionality of spacetime. These factors modify the blackbody spectrum of Hawking radiation, allowing the properties of the BH to be identified. [148,149]. To calculate the gray-body factor, the Regge–Wheeler potential is used to solve the wave equation of the emitted radiation. Using Eq. (33), an upper bound for the gray-body factor is obtained by [150,151].

$$T_l(\omega) \geq \operatorname{sech}^2\left(\frac{1}{2\omega}\int_{r_h}^{\infty} V_{\rm eff}(r)\frac{dr}{f(r)}\right), \tag{43}$$

where r_h refers to the horizon radius calculated in (5) and ω represents the frequency. Fig. 15 shows the gray-body boundaries in terms of frequency for a given set of initial values. The gray-body factor for perfect blackbody radiation is equal to one, but due to Hawking radiation, this value decreases. It is evident that, holding other parameters constant, a larger r_s (ρ_s) corresponds to a larger gray-body factor. At high frequencies, the gray-body factor bound approaches unity. This reflects the fact that energetic particles can effectively penetrate the centrifugal potential barrier with little suppression. In this regime, the spacetime geometry allows almost all incoming modes to be transmitted across the BH horizon. At lower frequencies the barrier plays a more important role. Our results show that as the scale radius increases, the transmission probability also increases, indicating that the structure of the surrounding dark matter halo modifies the effective potential in a way that facilitates particle passage. A similar trend is observed when varying the density parameter ρ_s: higher values of ρ_s also increase the gray-body bound. Thus, both r_s and ρ_s act to reduce the suppressive effect of the potential barrier at low frequencies, making spacetime more transparent to propagating modes.

The power emitted by a BH is the rate of energy radiation due to Hawking radiation [152,153]. It is quantified as the energy emitted per unit time and is expressed as [154]

$$P_l(\omega) = \frac{A}{8\pi^2} T_l(\omega) \frac{\omega^3}{\exp(\omega/T_{\rm H}) - 1}, \tag{44}$$

where $T_l(\omega)$ is the gray-body factor, ω is the frequency of the emitted particles, T_H refers to Hawking radiation, and A is the horizon area. Fig. 16 illustrates the emitted power for specific initial values. In both panels of Fig. 16, as r_s or ρ_s increase, the peak of the curve shifts to lower frequencies, meaning that the spectrum becomes redder. The height of the peak decreases with increasing halo parameters, meaning that the BH surrounded by a dark matter halo radiates less efficiently than an isolated Schwarzschild BH. As can be see from (7), the existence of the Hernquist dark matter halo lowers the Hawking temperature, and this lower Hawking temperature means that the BH radiates as a cooler blackbody that has less total power, and also that the peak of the emission power is shifted to lower frequencies.

The absorption cross section quantifies the probability of a particle being absorbed by a BH. For the lth mode it is calculated using (43) [155,156]

$$\sigma^l_{abs}(\omega) = \frac{\pi(2l+1)}{\omega^2}|T_l(\omega)|^2. \tag{45}$$

Fig. 17 represents the absorption cross-section curves for certain parameters. The absorption cross-section of a BH quantifies how efficiently it captures incoming radiation, whether scalar, electromagnetic, or gravitational waves. It encodes how the spacetime curvature and the event horizon interact with incident waves of different frequencies. At

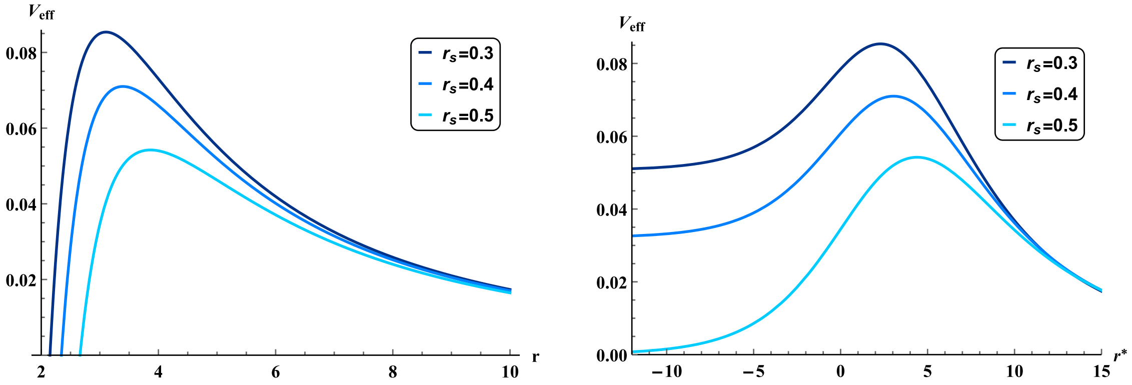

Fig. 13. Effective potential curves considering $M = 1$, $\rho_s = 0.5$ and $l = 2$. In the left panel, as a function of r, and in the right panel, varying r^*.

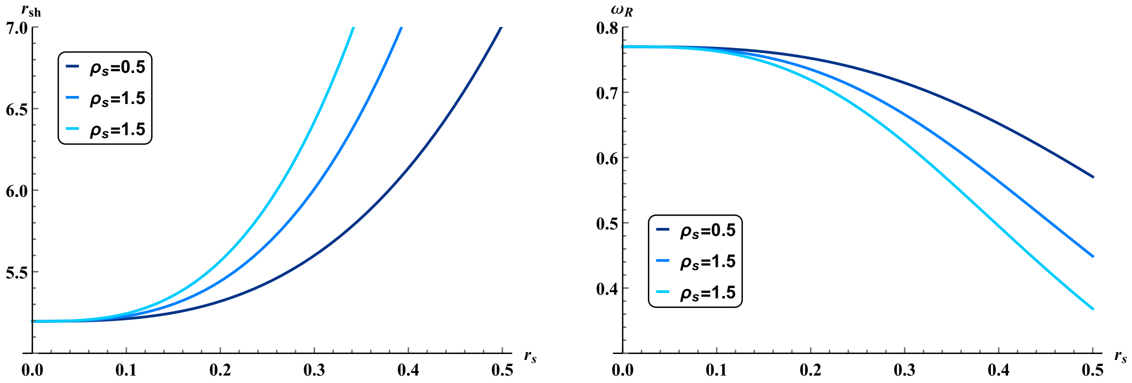

Fig. 14. Left panel: shadow radius in terms of r_s for three values of ρ_s, taking $M = 1$. Increasing the effects of the r_s or ρ_s parameters leads to an increase in the size of the BH's shadow. Left panel: the real part of the QNMs using the eikonal method and considering $M = 1$ and $l = 4$. It is evident that the real part of the quasinormal modes exhibits a behavior inversely related to the shadow.

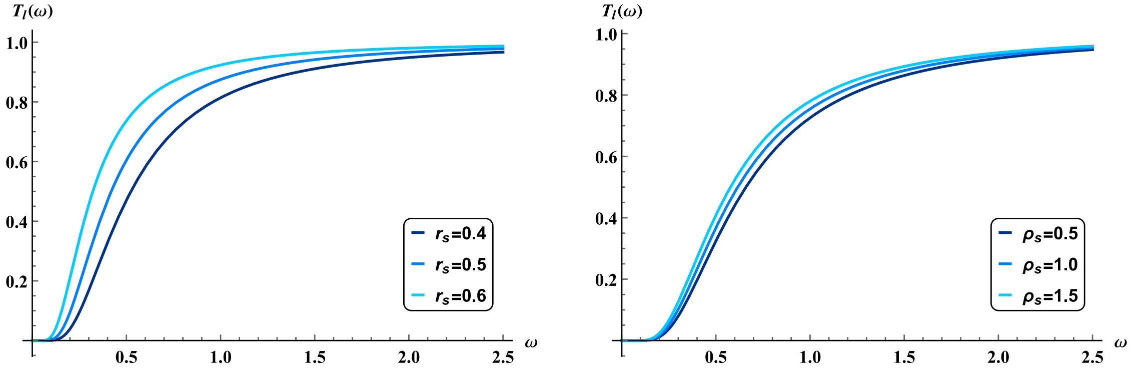

Fig. 15. Gray-body bounds considering $M = 1$, $l = 1$ and $s = 0$. On the left $\rho_s = 1$ and on the right $r_s = 0.3$. At low frequencies, an increase in the size of r_s or ρ_s leads to an increase in the magnitude of the gray-body bound. At high frequencies, the gray-body size approaches 1.

low frequencies ($\omega r_h \ll 1$), where ω is the wave frequency and r_h is the horizon radius, the wavelength of the incoming radiation is much larger than the size of the BH. In this regime, the wave cannot resolve the detailed structure of spacetime and instead perceives the BH as a point-like object. Consequently, only the spherically symmetric monopole mode ($l = 0$) contributes significantly, while higher multipoles are strongly suppressed. The absorption cross section therefore approaches the horizon area, $\sigma \to A_h = 4\pi r_h^2$. At high frequencies ($\omega r_h \gg 1$), the situation is very different: in this case the radiation wavelength is much smaller than the horizon radius, and the waves behave more similarly to classical particles. The absorption cross section is then governed by the capture of null geodesics near the photon sphere. In this limit, the cross section oscillates around the so-called geometrical optics limit, $\sigma = \pi b_c^2$, where b_c is the critical impact parameter characterizing the unstable circular photon orbit. These oscillations result from wave interference between radiation directly absorbed by the horizon and radiation temporarily trapped near the photon sphere before being finally absorbed.

The presence of a dark matter halo, modeled by a Hernquist profile (SBH–HDM spacetime), introduces additional modifications. The halo alters the spacetime metric by adding mass distributed outside the horizon. This has two clear consequences: in the low-frequency regime, the halo slightly expands the effective horizon radius, increasing its area. As a result, the low-frequency limit of the absorption cross section is larger than in the pure Schwarzschild case. The magnification increases with increasing halo density ρ_s or scale radius r_s. At high-frequency regime, the halo shifts the position of the photon sphere, thereby modifying the critical impact parameter b_c. This modifies the average

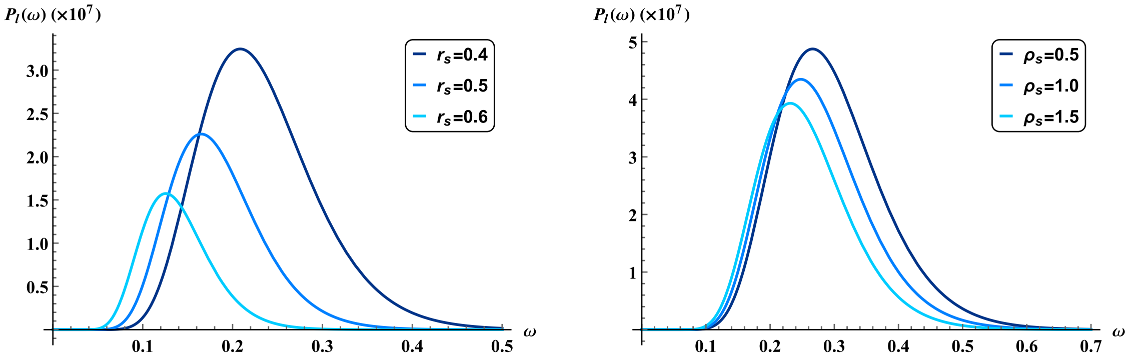

Fig. 16. Emitted power for the cases $M = 1$, $l = 1$ and $s = 0$. On the left $\rho_s = 1$ and on the right $r_s = 0.3$. An increase in the size of either of the parameters r_s or ρ_s increases the emitted power at a constant frequency, causing the maximum to be located at a higher frequency.

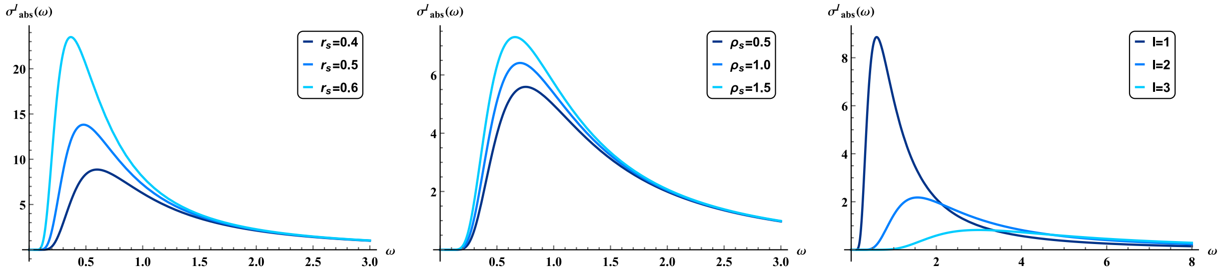

Fig. 17. Absorption cross section with parameters $M = 1$ and $s = 0$. On the left $\rho_s = 1$ and $l = 1$, in the center $r_s = 0.3$ and $l = 1$, on the right $\rho_s = 1$ and $r_s = 0.4$. An increase in the size of the parameters r_s or ρ_s improves the absorption size at a fixed frequency, shifting its maximum to a lower frequency. The effect of increasing l is exactly the opposite.

value of the high-frequency cross section. In general, the presence of the halo redistributes mass outward, reducing the capture efficiency of short-wavelength radiation. Compared to the Schwarzschild case, the average high frequency cross section is suppressed in the SBH–HDM background, and the oscillatory peaks are shifted to lower frequencies.

5. Topological characteristic

The thermodynamic properties derived in the previous section are not only determined by the local geometry of the BH horizon, but are also deeply constrained by its global topological features. In particular, the regularity of the Euclidean section fixes the Hawking temperature, while the entropy can often be expressed in terms of topological invariants, such as the Euler characteristic of the horizon manifold. This reflects the fact that BH thermodynamics is encoded in global structures of spacetime, rather than being purely local. The topological analysis performed in the next section provides a complementary perspective, revealing how the stability and phase structure of the BH are tied to the underlying topology of its horizon geometry.

In this section, we study some properties of BH from a topological perspective. To do so, we define a potential based on the investigated property, to which we assign vectors in spherical coordinates ϕ^i_r and ϕ^i_θ, normalized in the form $n^i_r = \phi^i_r/\|\phi\|$ and $n^i_\theta = \phi^i_\theta/\|\phi\|$, respectively [157–164]. Using these normalized vectors, the vector space of this potential can be visualized. There may be points in it where the vectors converge or diverge; these coordinates are the zero points of the vector space and can be considered topological defects [165–168]. Vector fields connect the geometry and topology of spacetime with thermodynamic properties, enabling a mathematical bridge between local thermodynamic quantities and global topological invariants, helping to interpret BH entropy and classify phase transitions in terms of topology. A topological charge, known as the winding number, can be assigned to each point in this space. This charge is calculated by examining the rotation of vectors around each point [168–170]. To do this, a closed contour c_i can be drawn around each point (θ, r_i) in this vector space. Using a variable transformation such as $r = a\cos\vartheta + r_i$ and $\theta = b\sin\vartheta + \frac{\pi}{2}$, the topological charge within each contour can be calculated from [171–173]

$$\Omega = w_i = \frac{1}{2\pi}\oint_{c_i} d(\arctan\frac{n_\theta}{n_r}). \tag{46}$$

If there are no zero points within this contour, the topological charge will be zero. However, if there is a zero point, rotating the vectors can indicate whether the topological charge is +1 or −1. [174–176]. The direction of the vectors around a zero point can be used to investigate the topological charge of the zero point, where the clockwise direction refers to a topological charge of −1 and the counterclockwise direction of the curve $\phi_\theta - \phi_r$ indicates a topological charge of +1 [177]. Based on the potential considered, conclusions can be drawn about it. In the following sections, three different potentials will be studied from a topological perspective.

5.1. Photon sphere

In Ref. [105], the photon sphere and the shadow of the BH were studied. In this section, to investigate the stability or instability of the photon sphere, a potential of the form [178–180]

$$H(r,\theta) = \frac{1}{\sin\theta}\sqrt{\frac{f(r)}{h(r)}}, \tag{47}$$

is defined, which can be represented in the vector space using the vectors [181–183]

$$\phi^H_r = \sqrt{f(r)}\partial_r H(r,\theta), \qquad \phi^H_\theta = \frac{1}{\sqrt{h(r)}}\partial_\theta H(r,\theta). \tag{48}$$

Fig. 18 shows the potential H at $\theta = \pi/2$ for $M = 1$, $r_s = 0.3$ and $\rho_s = 1$, which allows us to appreciate the existence of an extreme where the radial derivative of H becomes zero.

In Fig. 19, the normalized vector space representation of these vectors is shown for the case $M = 1$, $r_s = 0.3$ and $\rho_s = 1$. Two closed

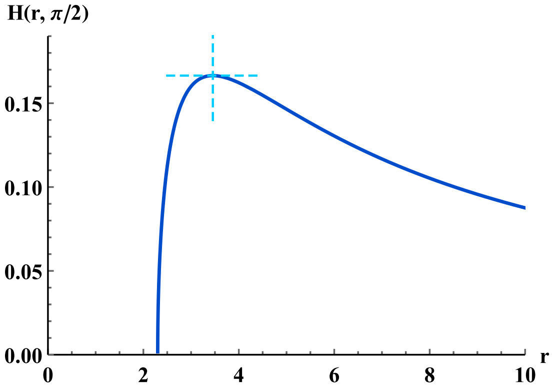

Fig. 18. The potential $H(r,\pi/2)$ as a function of r. Its extreme is at $\partial_r H\Big|_{r=r_c} = 0$.

contours, c_1 and c_2, are drawn around the zero point $r_1 = 3.45582$ and an arbitrary point $r_2 = 4.0$, respectively. Considering the rotation direction of the $\phi_r - \phi_\theta$ curve in the middle panel, as well as the variations of $\Delta\Omega$ in the right panel of Fig. 19, we conclude that the closed contour c_2 contains no topological charge, while the topological charge inside the contour c_1 is -1. This charge indicates the instability of the photon sphere located at r_1 [183].

5.2. Temperature

Another feature of BH that can be examined from a topological perspective is the BH Hawking temperature [184,185]. In Section 2 we studied the BH Hawking temperature and found that for $2\sqrt{\pi\rho_s}r_s > 1$, a phase transition to the BH Hawking temperature occurs. In this section, this transition will be examined using a topological approach. For this purpose, a thermodynamic potential is defined as [186–188]

$$\Phi = \frac{1}{\sin\theta} T_H, \tag{49}$$

which can be represented in the vector field defined by the following vectors [189–191]

$$\phi_r^{\Phi} = \partial_{r_h}\Phi, \qquad \phi_\theta^{\Phi} = \partial_\theta \Phi. \tag{50}$$

In Fig. 20, the vector space of potential Φ is illustrated for $r_s = 0.5$ and $\rho_s = 1$, and the zero point $r_1 = 0.82854$ can be seen. To analyze the topological charge of the zero point $r_1 = 0.82854$, we draw a closed contour c_1 around it and, choosing $a = b = 0.3$, calculate the topological charge using Eq. (46). The variations of Ω with respect to ϑ for the zero point r_1 on the closed contour c_1 are shown in Fig. 20. It is evident that this point has a topological charge of -1. This result is clearly seen in the central panel, considering the clockwise rotation of the $\phi_r - \phi_\theta$ curve. Therefore, we can conclude that by choosing $2\sqrt{\pi\rho_s}r_s > 1$, a phase transition occurs at the critical point r_c in the Hawking temperature of the BH, and this critical point is conventional [192].

5.3. Generalized free energy

The last property we will study from a topological perspective is the generalized free energy of the BH outside the shell surrounding the horizon. This energy is obtained from [193–195]

$$\mathcal{F} = M(r_h) - \frac{S}{\tau}, \tag{51}$$

where $M(r_h)$ is the mass of the BH as calculated in Eq. (6), τ is a parameter representing the inverse temperature of the BH, and S denotes the entropy of the BH, which using the Eqs. (6) and (7) is defined as

$$S = \int \frac{dM(r_h)}{T_H} dr_h = \pi r_h^2, \tag{52}$$

and is similar to the Schwarzschild BH entropy, although the dark matter parameters have effected the horizon radius as introduced in (5) [196,197]. The relevant vector space associated to the potential $\mathcal{F}$ is defined as [198–201]

$$\phi_r^{\mathcal{F}} = \partial_{r_h}\mathcal{F}, \qquad \phi_\theta^{\mathcal{F}} = -\cot\theta\csc\theta. \tag{53}$$

The zero points of this potential are located at $(r_c, \pi/2)$, where r_c is computed from $\partial_{r_h}\mathcal{F}\Big|_{r_h=r_c} = 0$. Therefore, by setting the radial derivative $\mathcal{F}$ to zero, we can find a relationship between τ and r_h, given by

$$\tau = \frac{4\pi r_h (r_h + r_s)^2}{(r_h + r_s)^2 - 4\pi\rho_s r_s^4}\Bigg|_{r_h=r_c}. \tag{54}$$

Fig. 21 shows the $r_h - \tau$ curve obtained from (54) for the values $r_s = 0.5$ and $\rho_s = 1$. The sign of the slope of this curve changes at $(0.82854, 18.75922)$, where it becomes infinite, with two branches appearing for $\tau > 18.75922$.

The first graph in Fig. 22 shows the vector space associated with the potential $\mathcal{F}$ for the parameters $r_s = 0.5$, $\rho_s = 1$ and $\tau = 30$. The two zero points $r_1 = 0.49556$ and $r_3 = 2.11263$ are highlighted in this space, along with the arbitrary point $r_2 = 1.30409$. To calculate the topological charge of these points, closed contours c_1, c_2, and c_3 have been drawn around the points r_1, r_2, and r_3, respectively. By choosing $a = b = 0.3$, we can calculate the integral from (46) for the specified points. In the middle panel of Fig. 22 we plot the curve $\phi_\theta - \phi_r$ to show the zero point r_h. The last graph in Fig. 22 shows the variation of Ω with respect to ϑ for the three contours c_1, c_2 and c_3. These contours correspond to topological charges of $\omega_1 = +1$, $\omega_2 = 0$ and $\omega_3 = -1$, respectively. This result is also evident from the middle panel of Fig. 22, taking into account the rotation direction of the $\phi_r - \phi_\theta$ curves. The vector space of the potential $\mathcal{F}$ contains two zero points, and the total topological charge is zero. This means that, from a topological classification perspective, this BH falls into the same class as the Reissner–Nordström BH [201].

6. Summary and conclusions

Considering a Schwarzschild BH immersed in a Hernquist dark matter halo (SBH–HDM), the mass of the system and the temperature at the horizon are determined. In some special cases of dark matter, there is some remnant mass, whereas in the absence of dark matter, when the horizon radius tends to zero, the horizon temperature tends to infinity. This is why many scientists are interested in investigating modified gravity to obtain remnant mass. The importance of remnant mass lies in the process of BH evaporation; at the end of this process, a special value of the mass is obtained, called the remnant mass, and in this case, the information is not lost. Our findings revealed that, for specific choices of r_s and ρ_s, a phase transition occurs at the BH's Hawking temperature, resulting in the emergence of a remnant mass. We established a criterion for parameter selection that facilitates the observation of both the remnant mass and the phase transition at the Hawking temperature. Next, we explore the influence of the Hernquist-type dark matter distribution on the matter in the thin accretion disk, quasi-normal modes in the eikonal limit, gray-body boundaries, and the thermodynamic topologies of BH. Initially, we investigate the motion of test particles, circular orbits, and radiative properties of the thin accretion disk around a BH within a Hernquist-type dark matter halo. A dark matter halo around a BH can push the ISCO outward, helping scientists study the BH's surroundings using X-ray emissions from accretion disks. Keeping r_s/M constant, an increase in $\rho_s M^2$, results in an increase in the total mass, leading to greater stability as

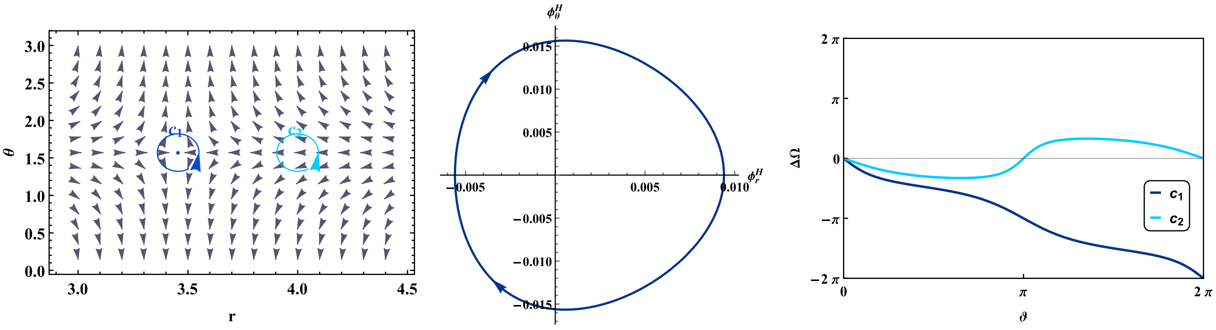

Fig. 19. Left panel: Vector space of the potential H with closed contours c_1 and c_2 drawn around $r_1 = 3.45582$ and $r_2 = 4.0$, respectively. Middle panel: The behavior of $\phi\theta - \phi r$ is shown for the zero point r_1. The clockwise direction indicates that $\omega_1 = 1$. Right panel: Variation of Ω in terms of ϑ, with $a = b = 0.3$. The topological charge inside the closed boundary c_1 is $w_1 = -1$, while the topological charge inside c_2 is $\omega_2 = 0$. The relevant parameters have been chosen to be $M = 1$, $r_s = 0.3$ and $\rho_s = 1$.

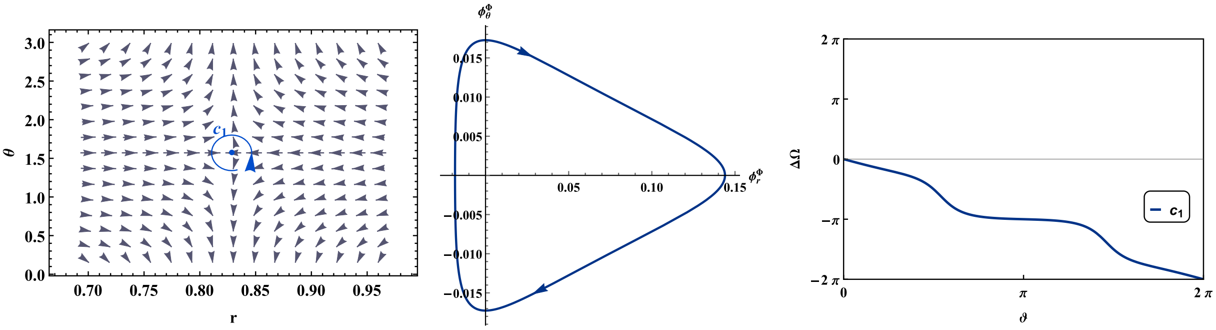

Fig. 20. Left panel: Vector space of the potential Φ containing a zero point at $r_1 = 0.82854$. Middle panel: Curve $\phi_\theta - \phi_r$ around zero point r_1. Clockwise direction means that $\omega_1 = 1$. Right panel: Changes in Ω as a function of ϑ for the closed contour c_1 ($a = b = 0.3$), indicating a topological charge of -1. The parameters are chosen as $r_s = 0.5$ and $\rho_s = 1$.

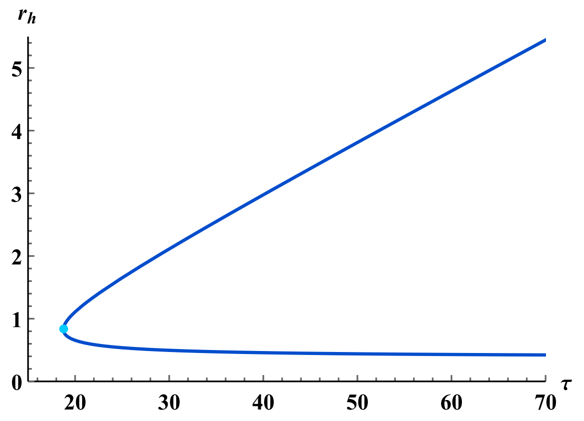

Fig. 21. $r_h - \tau$ curve (54) for the values $r_s = 0.5$ and $\rho_s = 1$. At $\tau = 18.75922$ the sign of the slope of the curve changes.

the particle positions itself at a larger radius. We observe that, holding one parameter of the dark matter halo constant, an increase in the other leads to a reduction in energy E, while the angular momentum L and angular velocity Ω increase with respect to the corresponding values in the Schwarzschild BH case. Moreover, at smaller radii, the impact of the dark matter model parameters r_s and ρ_s decreases significantly. In the equatorial plane, we calculated the ISCO radius and found that an increase in either r_s or ρ_s results in an expansion of this radius. We find that, for small r_s, the radiative efficiency increases with rising halo density ρ_s, while for larger r_s, this trend is reversed and the efficiency decreases as ρ_s increases. We also observed that an increase in the parameter ρ_s leads to a shift in this trend at a smaller r_s. Next, we analyze the thin accretion disk in the SBH–HDM scenario as the primary instrument for studying the surrounding spacetime geometry. Using the steady-state Novikov–Thorne model, we numerically calculate key disk properties, including the energy flux and temperature distribution, the differential luminosity, and the spectral luminosity, for geometrically thin accretion disks. These results were subsequently compared with those obtained for a Schwarzschild BH in the framework of general relativity.

Our analysis revealed that the Schwarzschild BH exhibits a higher energy flux, while an increase in r_s causes this value to decrease and shifts its peak to a larger radius. We examined the radiation temperature and observed a decrease compared to the Schwarzschild BH. In our study of the differential luminosity, we observed a significant increase with increasing r_s, and the maximum now occurs at a larger radius.

In flat spacetime, as $r/M \to \infty$, the redshift factor approaches 1, regardless of the dark matter parameters. However, at lower r/M, increasing r_s/M decreases the redshift factor, resulting in $\tilde{g}^{\mathrm{SBH\text{-}-HDM}}(r) < \tilde{g}^{\mathrm{SBH}}(r)$. The redshift factor can be determined directly through experiments by measuring the frequency shift of a known spectral line or clock signal between two different gravitational potentials. By analyzing these data and using the root-mean-square method to adjust theoretical predictions, it is possible to determine the best values for r_s and ρ_s.

We then delve deeper into the BH's quasi-normal modes, investigating the interaction between them and the BH shadow within the eikonal regime. We have shown that, in the eikonal regime, the Lyapunov exponent of the null geodesics is related to the imaginary part of the QNM, which can illustrate the stability or instability of the system. The shadow can be obtained by taking the inverse of the real part of the QNM, which is comparable with the other methods. We also note that while increasing the effects of dark matter parameters broadens the BH shadow, it leads to a decrease in the magnitude of the real part

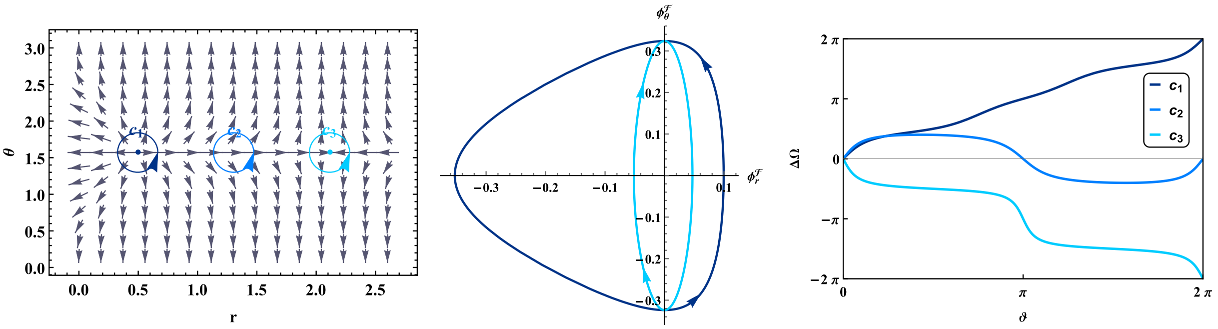

Fig. 22. Left panel: Vector space of the potential $\mathcal{F}$. The zero points $r_1 = 0.49556$ and $r_3 = 2.11263$ are indicated, as well as an arbitrary point at $r_2 = 1.30409$. Middle panel: ϕ_θ versus ϕ_r for zero points r_1 and r_2. The direction of the curves indicates that $\omega_1 = 1$ and $\omega_3 = -1$. Right panel: The variation of Ω with respect to ϑ under the assumption $a = b = 0.3$ is shown for the closed contours c_1, c_2 and c_3, which enclose the points r_1, r_2 and r_3, respectively. The corresponding topological charge of these contours is given by $\omega_1 = 1$, $\omega_2 = 0$ and $\omega_3 = -1$. The parameters are set as $r_s = 0.5$, $\rho_s = 1$ and $\tau = 30$.

of the quasinormal modes. In particular, we find that holding other parameters constant while increasing r_s leads to an expansion of the BH shadow and a reduction in the real part of the quasi-normal modes. We then examine the scattering surrounding the BH, analyzing the gray-body factor, the emitted power, and the absorption cross section. Our results indicated that an increase in r_s (ρ_s), with other parameters constant, enhances both the gray-body factor and the absorption, shifting the absorption peak to lower frequencies. On the contrary, this increase results in a decrease in the emitted power, shifting its peak toward lower frequencies. In the final segment, we investigate the BH's photon sphere from a topological perspective, revealing that this BH possesses an unstable photon sphere, which contributes to the formation of its shadow. Finally, we examine the BH's thermodynamic potentials from a topological perspective. Vector fields connect the shape of spacetime to thermodynamic properties, helping us understand the entropy of BH and classify phase changes through their topological characteristics. We explore the phase transition at the Hawking temperature for $2\sqrt{\pi\rho_s}r_s > 1$ and identify this critical point as conventional. Furthermore, we find that the generalized out-of-shell free energy of the BH exhibits two distinct phase transitions, while the topological charge in the vector space of this thermodynamic potential is zero. This allows us to precisely classify the topological nature of this BH, placing it within the realm of Reissner–Nordström BHs. Extending the present analysis to the class of new rotating spacetimes (considered astrophysically more realistic than those admitting a smooth and asymptotically flat expansion) represents a compelling direction for future research, in which we are currently making rapid progress.

CRediT authorship contribution statement

Luis M. Nieto: Writing – review & editing, Writing – original draft, Visualization, Validation, Supervision, Resources, Project administration, Methodology, Investigation, Funding acquisition, Formal analysis, Conceptualization. **Farokhnaz Hosseinifar:** Writing – review & editing, Writing – original draft, Visualization, Validation, Supervision, Software, Resources, Methodology, Investigation, Formal analysis, Data curation. **Kuantay Boshkayev:** Writing – review & editing, Writing – original draft, Visualization, Validation, Supervision, Software, Resources, Methodology, Investigation, Formal analysis, Data curation, Conceptualization. **Soroush Zare:** Writing – review & editing, Writing – original draft, Visualization, Validation, Supervision, Software, Resources, Methodology, Investigation, Formal analysis, Data curation, Conceptualization. **Hassan Hassanabadi:** Writing – review & editing, Writing – original draft, Visualization, Validation, Supervision, Software, Resources, Methodology, Investigation, Formal analysis, Data curation, Conceptualization.

Declaration of competing interest

The authors declare the following financial interests/personal relationships which may be considered as potential competing interests: L.M. Nieto, H. Hassanabadi and S. Zare report financial support provided by Spain Ministry of Science and Innovation, by European Union and by Junta de Castlla y León (Consejeria de Educacion). H. Hassanabadi is supported by FoS UHK from Czech Republic.

Acknowledgments

The authors would like to express their gratitude to the referees for their constructive comments. The research of L.M.N., S.Z. and H.H. was supported by the Q-CAYLE project, funded by the European Union-Next Generation UE/MICIU/Plan de Recuperacion, Transformacion y Resiliencia/Junta de Castilla y Leon (PRTRC17.11), and also by project PID2023-148409NB-I00, funded by MICIU/AEI/10.13039/501100011033. Financial support of the Department of Education of the Junta de Castilla y Leon and FEDER Funds is also gratefully acknowledged (Reference: CLU-2023-1-05). Additionally, H. H. is grateful to Excellence project FoS UHK 2203/2025-2026 for the financial support.

Data availability

No data was used for the research described in the article.

References

[1] C. Bambi, Black Holes: a Laboratory for Testing Strong Gravity, vol. 10, Springer, 2017.
[2] I. Novikov, V. Frolov, Physics of Black Holes, vol. 27, Springer Science & Business Media, 2013.
[3] M. Begelman, M. Rees, Gravity's Fatal Attraction: Black Holes in the Universe, Cambridge University Press, 2020.
[4] J.C. Wheeler, Cosmic Catastrophes: Exploding Stars, Black Holes, and Mapping the Universe, Cambridge University Press, 2007.
[5] R.M. Wald, Space, Time, and Gravity: The Theory of the Big Bang and Black Holes, University of Chicago Press, 1992.
[6] B.P. Abbott, R. Abbott, T.D. Abbott, M.R. Abernathy, F. Acernese, K. Ackley, C. Adams, T. Adams, P. Addesso, R.X. Adhikari, et al., Phys. Rev. Lett. 116 (2016) 061102.
[7] R. Abbott, T. Abbott, F. Acernese, K. Ackley, C. Adams, N. Adhikari, R. Adhikari, V. Adya, C. Affeldt, D. Agarwal, et al., Phys. Rev. X 13 (2023) 041039.
[8] K. Akiyama, A. Alberdi, W. Alef, K. Asada, R. Azulay, A. Baczko, D. Ball, M. Baloković, J. Barrett, E.H.T. Collaboration, et al., Astrophys. J. Lett. 875 (2019) L1.
[9] K. Akiyama, J.C. Algaba, A. Alberdi, W. Alef, R. Anantua, K. Asada, R. Azulay, A.-K. Baczko, D. Ball, M. Baloković, et al., Astrophys. J. Lett. 910 (2021) L12.
[10] E.H.T. Collaboration, et al., 930, Astrophys. J. Lett. (2022) L12.
[11] M. Bauböck, J. Dexter, R. Abuter, A. Amorim, J. Berger, H. Bonnet, W. Brandner, Y. Clénet, V.C. Du Foresto, P. de Zeeuw, et al., Astron. Astrophys. 635 (2020) A143.

[12] D. Richstone, E. Ajhar, R. Bender, G. Bower, A. Dressler, S. Faber, A. Filippenko, K. Gebhardt, R. Green, L. Ho, et al., 1998, arXiv preprint astro-ph/9810378.
[13] T.M. Heckman, P.N. Best, Annu. Rev. Astron. Astrophys. 52 (2014) 589.
[14] A. Cattaneo, S. Faber, J. Binney, A. Dekel, J. Kormendy, R. Mushotzky, A. Babul, P. Best, M. Brüggen, A. Fabian, et al., Nature 460 (2009) 213.
[15] T. Di Matteo, J. Colberg, V. Springel, L. Hernquist, D. Sijacki, Astrophys. J. 676 (2008) 33.
[16] J. Kormendy, L.C. Ho, Annu. Rev. Astron. Astrophys. 51 (2013) 511.
[17] M. Morscher, B. Pattabiraman, C. Rodriguez, F.A. Rasio, S. Umbreit, Astrophys. J. 800 (2015) 9.
[18] D.N. Spergel, Science 347 (2015) 1100.
[19] B. Clegg, Dark Matter and Dark Energy: The Hidden 95% of the Universe, Icon Books, 2019.
[20] G. Bertone, D. Hooper, Rev. Modern Phys. 90 (2018) 045002.
[21] V.C. Rubin, Dark Universe: Matter, Energy Gravity, vol. 1, 2004.
[22] F. Zwicky, Helv. Phys. Acta 6 (1933) 110–127.
[23] S.M. Fall, G. Efstathiou, Mon. Not. R. Astron. Soc. 193 (1980) 189.
[24] S.D. White, M.J. Rees, Mon. Not. R. Astron. Soc. 183 (1978) 341.
[25] J.C. Kapteyn, A Source Book in Astronomy and Astrophysics, 1900–1975, Harvard University Press, 1979, pp. 542–549.
[26] E. Battaner, E. Florido, 2000, arXiv preprint astro-ph/0010475.
[27] M. Persic, P. Salucci, F. Stel, Mon. Not. R. Astron. Soc. 281 (1996) 27.
[28] M.A. Karim, J. Aguilar, S. Ahlen, S. Alam, L. Allen, C. Allende Prieto, O. Alves, A. Anand, U. Andrade, E. Armengaud, et. al, 2025, arXiv e-prints, arXiv.
[29] E. Silva, M.A. Sabogal, M. Scherer, R.C. Nunes, E. Di Valentino, S. Kumar, Phys. Rev. D 111 (2025) 123511.
[30] J.C. Hill, E. Calabrese, S. Aiola, N. Battaglia, B. Bolliet, S.K. Choi, M.J. Devlin, A.J. Duivenvoorden, J. Dunkley, S. Ferraro, et. al, Phys. Rev. D 105 (2022) 123536.
[31] L. Randall, Nature 557 (2018) S6.
[32] R.H. Wechsler, J.L. Tinker, Annu. Rev. Astron. Astrophys. 56 (2018) 435.
[33] M.S. Turner, Phys. Scr. 1991 (1991) 167.
[34] S. Capozziello, M. De Laurentis, Ann. Phys., Lpz. 524 (2012) 545.
[35] S.W. Randall, M. Markevitch, D. Clowe, A.H. Gonzalez, M. Bradač, Astrophys. J. 679 (2008) 1173.
[36] V. Trimble, Annu. Rev. Astron. Astrophys. 25 (1987) 425.
[37] M. Kunz, S. Nesseris, I. Sawicki, Phys. Rev. D 94 (2016) 023510.
[38] R. Konoplya, Phys. Lett. B 795 (2019) 1.
[39] S. Ghosh, A. Bhadra, Eur. Phys. J. C 75 (2015) 1.
[40] E. Oks, New Astron. Rev. 93 (2021) 101632.
[41] V. Sahni, Phys. Early Universe 141 (2004).
[42] R. Konoplya, A. Zhidenko, Astrophys. J. 933 (2022) 166.
[43] J.R. Primack, 1997, arXiv preprint astro-ph/9707285.
[44] B. Ratra, M.S. Vogeley, Publ. Astron. Soc. Pac. 120 (2008) 235.
[45] P. Dayal, A. Ferrara, Phys. Rep. 780 (2018) 1.
[46] Z. Shen, A. Wang, Y. Gong, S. Yin, Phys. Lett. B 855 (2024) 138797.
[47] J. Zavala, C.S. Frenk, Galaxies 7 (2019) 81.
[48] V. Rubakov, 2019, arXiv preprint arXiv:1912.04727.
[49] G. Bertone, Particle Dark Matter: Observations, Models and Searches, Cambridge University Press, 2010.
[50] K. Short, 2022.
[51] B. Carr, Annu. Rev. Astron. Astrophys. 32 (1994) 531–590.
[52] C.J. Hogan, J.J. Dalcanton, Phys. Rev. D 62 (2000) 063511.
[53] L. Hernquist, Astrophys. J. Part 1 (ISSN: 0004-637X) 356 (1990) 359–364.
[54] M. Ghosh, Modern Phys. Lett. A 39 (2024) 2450142.
[55] L. Sadeghian, F. Ferrer, C.M. Will, Phys. Rev. D—Particles Fields Gravit. Cosmol. 88 (2013) 063522.
[56] E. Figueiredo, A. Maselli, V. Cardoso, Phys. Rev. D 107 (2023) 104033.
[57] J.L.P. Kamermans, A.R.A. Wierda, Mon. Not. R. Astron. Soc. 539 (2025) 135.
[58] L. Pezzella, K. Destounis, A. Maselli, V. Cardoso, Phys. Rev. D 111 (2025) 064026.
[59] K.-i. Maeda, V. Cardoso, A. Wang, Phys. Rev. D 111 (2025) 044060.
[60] N. Speeney, E. Berti, V. Cardoso, A. Maselli, Phys. Rev. D 109 (2024) 084068.
[61] A. Uniyal, R.C. Pantig, A. Övgün, Phys. Dark Universe 40 (2023) 101178.
[62] G. Lambiase, R.C. Pantig, D.J. Gogoi, A. Övgün, Eur. Phys. J. C 83 (2023) 679.
[63] M. Khodadi, G. Lambiase, Phys. Rev. D 106 (2022) 104050.
[64] A. Allahyari, M. Khodadi, S. Vagnozzi, D.F. Mota, J. Cosmol. Astropart. Phys. 2020 (2020) 003.
[65] G. Panotopoulos, Á. Rincón, I. Lopes, Phys. Rev. D 103 (2021) 104040.
[66] B.E. Panah, S. Zare, H. Hassanabadi, Eur. Phys. J. C 84 (2024) 259.
[67] L. Meng, Z. Xu, M. Tang, Eur. Phys. J. C 85 (2025) 306.
[68] M.-H. Wu, H. Guo, X.-M. Kuang, Phys. Rev. D 107 (2023) 064033.
[69] Y. Meng, X.-M. Kuang, X.-J. Wang, B. Wang, J.-P. Wu, Phys. Rev. D 108 (2023) 064013.
[70] Y. Meng, X.-M. Kuang, X.-J. Wang, B. Wang, J.-P. Wu, Eur. Phys. J. C 84 (2024) 305.
[71] Z.-Y. Tu, T. Zhu, A. Wang, Phys. Rev. D 108 (2023) 024035.
[72] S. Zare, L.M. Nieto, X.-H. Feng, S.-H. Dong, H. Hassanabadi, J. Cosmol. Astropart. Phys. 2024 (2024) 041.
[73] S. Wu, B. Wang, Z. Long, H. Chen, Phys. Dark Universe 44 (2024) 101455.
[74] R.C. Pantig, A. Övgün, J. Cosmol. Astropart. Phys. 2022 (2022) 056.
[75] S. Capozziello, S. Zare, D. Mota, H. Hassanabadi, J. Cosmol. Astropart. Phys. 2023 (2023) 027.
[76] S. Capozziello, S. Zare, H. Hassanabadi, 2023, arXiv preprint arXiv:2311.12896.
[77] Y. Sekhmani, S. Zare, L. Nieto, H. Hassanabadi, K. Boshkayev, 2025, arXiv preprint arXiv:2501.10874.
[78] Z. Xu, X. Hou, X. Gong, J. Wang, J. Cosmol. Astropart. Phys. 2018 (2018) 038.
[79] N.I. Shakura, R.A. Sunyaev, Astron. Astrophys. 24 (1973) 337–355.
[80] I.D. Novikov, K.S. Thorne, Black Holes (Les Astres Occlus) 1 (1973) 343.
[81] D.N. Page, K.S. Thorne, Astrophys. J. 191 (1974) 499–506.
[82] K.S. Thorne, Astrophys. J. 191 (1974) 507–520.
[83] S. Kato, J. Fukue, S. Mineshige, Black-Hole Accretion Disks: Towards a New Paradigm, Kyoto University Press, 2008.
[84] K. Jusufi, A. Anand, S. Saghafi, B. Cuadros-Melgar, K. Nozari, Eur. Phys. J. C 85 (2025) 1.
[85] C. Liu, S. Yang, Q. Wu, T. Zhu, J. Cosmol. Astropart. Phys. 2022 (2022) 034.
[86] T. Harko, Z. Kovács, F.S. Lobo, Phys. Rev. D—Particles Fields Gravit. Cosmol. 80 (2009) 044021.
[87] S. Chen, J. Jing, Phys. Lett. B 704 (2011) 641.
[88] T. Harko, Z. Kovács, F.S. Lobo, Classical Quantum Gravity 28 (2011) 165001.
[89] T. Johannsen, Phys. Rev. D—Particles Fields Gravit. Cosmol. 87 (2013) 124010.
[90] P. Mach, E. Malec, J. Karkowski, Phys. Rev. D—Particles Fields Gravit. Cosmol. 88 (2013) 084056.
[91] J. Karkowski, E. Malec, Phys. Rev. D—Particles Fields Gravit. Cosmol. 87 (2013) 044007.
[92] F. Yuan, R. Narayan, Annu. Rev. Astron. Astrophys. 52 (2014) 529.
[93] K. Boshkayev, A. Idrissov, O. Luongo, D. Malafarina, Mon. Not. R. Astron. Soc. 496 (2020) 1115.
[94] Y. Kurmanov, K. Boshkayev, T. Konysbayev, O. Luongo, N. Saiyp, A. Urazalina, G. Ikhsan, G. Suliyeva, Phys. Dark Universe 46 (2024) 101566.
[95] Y. Kurmanov, K. Boshkayev, T. Konysbayev, M. Muccino, O. Luongo, A. Urazalina, A. Dalelkhankyzy, F. Belissarova, M. Alimkulova, Phys. Dark Universe 48 (2025) 101917.
[96] M. Heydari-Fard, M. Heydari-Fard, H.R. Sepangi, Eur. Phys. J. C 81 (2021) 473.
[97] R.K. Karimov, R. Izmailov, A. Bhattacharya, K. Nandi, Eur. Phys. J. C 78 (2018) 1.
[98] C. Bambi, Astrophys. J. 761 (2012) 174.
[99] G. Gyulchev, P. Nedkova, T. Vetsov, S. Yazadjiev, Eur. Phys. J. C 81 (2021) 1.
[100] T.-Y. He, Z. Cai, R.-J. Yang, Eur. Phys. J. C 82 (2022) 1067.
[101] C. Liu, T. Zhu, Q. Wu, Chin. Phys. C 45 (2021) 015105.
[102] L. Jiao, R. Yang, Eur. Phys. J. C 77 (2017) 1.
[103] G. Murtaza, A. Ditta, T. Naseer, G. Mustafa, S. Maurya, A. Ghaffar, F. Javed, J. High Energy Astrophys. 44 (2024) 279.
[104] Y.-H. Jiang, T. Wang, Phys. Rev. D 110 (2024) 103009.
[105] S.K. Jha, 2025, arXiv preprint arXiv:2503.19938.
[106] H. Mo, F. Van den Bosch, S. White, Galaxy Formation and Evolution, Cambridge University Press, 2010.
[107] S.W. Hawking, Nature 248 (1974) 30.
[108] S.W. Hawking, D.N. Page, Comm. Math. Phys. 87 (1983) 577.
[109] K. Fredenhagen, R. Haag, Comm. Math. Phys. 127 (1990) 273.
[110] A. Delhom, C.F. Macedo, G.J. Olmo, L.C. Crispino, Phys. Rev. D 100 (2019) 024016.
[111] S.B. Giddings, Phys. Rev. D 46 (1992) 1347.
[112] S.-H. Dong, F. Hosseinifar, F. Studnička, H. Hassanabadi, Phys. Lett. B 860 (2025) 139182.
[113] L. Berezhiani, G. Chkareuli, C. De Rham, G. Gabadadze, A. Tolley, Phys. Rev. D—Particles Fields Gravit. Cosmol. 85 (2012) 044024.
[114] G. Gibbons, Classical Quantum Gravity 33 (2015) 025004.
[115] V. Perlick, O.Y. Tsupko, G.S. Bisnovatyi-Kogan, Phys. Rev. D 97 (2018) 104062.
[116] V. Perlick, O.Y. Tsupko, Phys. Rep. 947 (2022) 1.
[117] T. Ono, H. Asada, Universe 5 (2019) 218.
[118] A. Bakopoulos, T. Karakasis, N.E. Mavromatos, T. Nakas, E. Papantonopoulos, Phys. Rev. D 110 (2024) 024014.
[119] Z. Shen, A. Wang, S. Yin, Phys. Lett. B 862 (2025) 139300.
[120] E. Kurmanov, K. Boshkayev, R. Giambò, T. Konysbayev, O. Luongo, D. Malafarina, H. Quevedo, Astrophys. J. 925 (2022) 210.
[121] S. Patra, B.R. Majhi, 2025, arXiv preprint arXiv:2501.07456.
[122] L.G. Collodel, D.D. Doneva, S.S. Yazadjiev, Astrophys. J. 910 (2021) 52.
[123] K. Nozari, S. Saghafi, F. Aliyan, Eur. Phys. J. C 83 (2023) 449.
[124] K. Nozari, S. Saghafi, M. Hassani, J. High Energy Astrophys. 45 (2025) 214.
[125] K. Nozari, S. Saghafi, M. Hajebrahimi, K. Jusufi, Phys. Dark Universe 49 (2025) 102027.
[126] S.C. Noble, J.H. Krolik, J.F. Hawley, Astrophys. J. 692 (2009) 411.
[127] J.E. McClintock, R. Narayan, S.W. Davis, L. Gou, A. Kulkarni, J.A. Orosz, R.F. Penna, R.A. Remillard, J.F. Steiner, Classical Quantum Gravity 28 (2011) 114009.
[128] F.H. Zuluaga, L.A. Sánchez, Eur. Phys. J. C 81 (2021) 1.
[129] K. Boshkayev, T. Konysbayev, E. Kurmanov, O. Luongo, D. Malafarina, H. Quevedo, Phys. Rev. D 104 (2021) 084009.
[130] K. Boshkayev, T. Konysbayev, Y. Kurmanov, O. Luongo, M. Muccino, A. Taukenova, A. Urazalina, Eur. Phys. J. C 84 (2024) 230.

[131] R. D'Agostino, R. Giambo, O. Luongo, Phys. Rev. D 107 (2023) 043032.
[132] K. Boshkayev, T. Konysbayev, Y. Kurmanov, O. Luongo, D. Malafarina, Astrophys. J. 936 (2022) 96.
[133] A. Fernandez-Soto, K.M. Lanzetta, H.-W. Chen, S.M. Pascarelle, N. Yahata, Astrophys. J. Suppl. Ser. 135 (2001) 41.
[134] C. Wang, Ann. Phys., Lpz. 523 (2011) 239.
[135] L.D. Landau, The Classical Theory of Fields, vol.2, Elsevier, 2013.
[136] P.G. LeFloch, Y. Ma, Comm. Math. Phys. 346 (2016) 603.
[137] R.A. Konoplya, A. Zhidenko, Rev. Modern Phys. 83 (2011) 793.
[138] K.S. Thorne, C.W. Misner, J.A. Wheeler, Gravitation, Freeman San Francisco, 2000.
[139] R.A. Konoplya, Phys. Rev. D 66 (2002) 044009.
[140] T. Regge, J.A. Wheeler, Phys. Rev. 108 (1957) 1063.
[141] N. Heidari, H. Hassanabadi, Phys. Lett. B 839 (2023) 137814.
[142] K.S. Virbhadra, G.F. Ellis, Phys. Rev. D 62 (2000) 084003.
[143] K.S. Virbhadra, G.F. Ellis, Phys. Rev. D 65 (2002) 103004.
[144] V. Cardoso, A.S. Miranda, E. Berti, H. Witek, V.T. Zanchin, Phys. Rev. D—Particles Fields Gravit. Cosmol. 79 (2009) 064016.
[145] P. Kanti, Internat. J. Modern Phys. A 19 (2004) 4899.
[146] F. Gray, M. Visser, Universe 4 (2018) 93.
[147] T. Harmark, J. Natario, R. Schiappa, 2010.
[148] P. Kanti, T. Pappas, N. Pappas, Phys. Rev. D 90 (2014) 124077.
[149] R.A. Konoplya, A.F. Zinhailo, Phys. Lett. B 810 (2020) 135793.
[150] P. Boonserm, T. Ngampitipan, P. Wongjun, Eur. Phys. J. C 79 (2019) 1.
[151] S.K. Jha, 2024, arXiv preprint arXiv:2404.15808.
[152] C.M. Harris, P. Kanti, J. High Energy Phys. 2003 (2003) 014.
[153] P. Kanti, E. Winstanley, Quantum Aspects of Black Holes, Springer, 2014, pp. 229–265.
[154] Y.-G. Miao, Z.-M. Xu, Phys. Lett. B 772 (2017) 542.
[155] C. Doran, A. Lasenby, S. Dolan, I. Hinder, Phys. Rev. D—Particles Fields Gravit. Cosmol. 71 (2005) 124020.
[156] Y. Décanini, G. Esposito-Farese, A. Folacci, Phys. Rev. D—Particles Fields Gravit. Cosmol. 83 (2011) 044032.
[157] M.A.S. Afshar, J. Sadeghi, Chin. Phys. C (2024).
[158] A. Malik, A. Mehmood, M.U. Shahzad, Ann. Physics 463 (2024) 169617.
[159] F. Hosseinifar, S. Mamedov, F. Studnička, H. Hassanabadi, 2025, arXiv preprint arXiv:2503.03260.
[160] W. Liu, D. Wu, J. Wang, 2024, arXiv preprint arXiv:2412.18083.
[161] C. Fang, J. Jiang, M. Zhang, J. High Energy Phys. 2023 (2023) 1.
[162] J. Sadeghi, S.N. Gashti, M.R. Alipour, M.A.S. Afshar, Ann. Physics 455 (2023) 169391.
[163] S.-P. Wu, S.-W. Wei, Phys. Rev. D 110 (2024) 024054.
[164] D. Wu, W. Liu, S.-Q. Wu, R.B. Mann, Phys. Rev. D 111 (2025) L061501.
[165] Z.-Y. Fan, Phys. Rev. D 107 (2023) 044026.
[166] S.-W. Wei, Y.-X. Liu, R.B. Mann, Phys. Rev. D 110 (2024) L081501.
[167] Z.-Q. Chen, S.-W. Wei, Eur. Phys. J. C 84 (2024) 1.
[168] D. Wu, Phys. Rev. D 107 (2023) 024024.
[169] A. Mehmood, M.U. Shahzad, 2023, arXiv preprint arXiv:2310.09907.
[170] Y.-S. Wang, Z.-M. Xu, B. Wu, Chin. Phys. C 48 (2024) 095101.
[171] C. Liu, J. Wang, Phys. Rev. D 107 (2023) 064023.
[172] A. Mehmood, N. Alessa, M.U. Shahzad, E.E. Zotos, Nuclear Phys. B 1006 (2024) 116653.
[173] M. Yasir, X. Tiecheng, A. Jawad, Eur. Phys. J. C 84 (2024) 946.
[174] Y. Du, X. Zhang, 2023, arXiv preprint arXiv:2302.11189.
[175] S.-W. Wei, Y.-X. Liu, Phys. Rev. D 107 (2023) 064006.
[176] P.K. Yerra, C. Bhamidipati, Phys. Rev. D 105 (2022) 104053.
[177] M. Rizwan, M. Jamil, M. Moughal, 2025, arXiv preprint arXiv:2501.04739.
[178] M.R. Alipour, M.A.S. Afshar, S.N. Gashti, J. Sadeghi, 2024, arXiv preprint arXiv:2410.14352.
[179] S.N. Gashti, I. Sakallı, B. Pourhassan, 2024, arXiv preprint arXiv:2410.14492.
[180] R.C. Pantig, A. Övgün, 2025, arXiv preprint arXiv:2503.18585.
[181] Y. Sekhmani, S.N. Gashti, M.A.S. Afshar, M.R. Alipour, J. Sadeghi, B. Pourhassan, J. Rayimbaev, 2024, arXiv preprint arXiv:2409.04997.
[182] M.U. Shahzad, N. Alessa, A. Mehmood, S. Mamedov, Internat. J. Theoret. Phys. 64 (2025) 1.
[183] S.-W. Wei, Phys. Rev. D 102 (2020) 064039.
[184] C.W. Robson, L. Di Mauro Villari, F. Biancalana, Phys. Rev. D 99 (2019) 044042.
[185] C.W. Robson, L.D.M. Villari, F. Biancalana, 2019, arXiv preprint arXiv:1903.04627.
[186] P.K. Yerra, C. Bhamidipati, S. Mukherji, Journal of Physics: Conference Series, vol. 2667, IOP Publishing, 2023, 012031.
[187] Z.-Q. Chen, S.-W. Wei, Nuclear Phys. B 996 (2023) 116369.
[188] K. Bhattacharya, K. Bamba, D. Singleton, Phys. Lett. B 854 (2024) 138722.
[189] I. Jeon, B.-H. Lee, W. Lee, M. Mishra, Phys. Rev. D 111 (2025) 064006.
[190] H. Chen, D. Wu, M.-Y. Zhang, H. Hassanabadi, Z.-W. Long, Phys. Dark Universe 46 (2024) 101617.
[191] M.S. Ali, H. El Moumni, J. Khalloufi, K. Masmar, Ann. Physics 465 (2024) 169679.
[192] S.-W. Wei, Y.-X. Liu, Phys. Rev. D 105 (2022) 104003.
[193] S.N. Gashti, 2024, arXiv preprint arXiv:2412.00889.
[194] D. Wu, S.-Y. Gu, X.-D. Zhu, Q.-Q. Jiang, S.-Z. Yang, J. High Energy Phys. 2024 (2024) 1.
[195] T.N. Hung, C.H. Nam, Eur. Phys. J. C 83 (2023) 582.
[196] K. Nozari, S. Saghafi, A. Damavandi Kamali, Astrophys. Space Sci. 357 (2015) 140.
[197] S. Saghafi, K. Nozari, M. Hajebrahimi, Int. J. Geom. Methods Mod. Phys. 18 (2021) 2150024.
[198] M. Rizwan, K. Jusufi, Eur. Phys. J. C 83 (2023) 944.
[199] B. Eslam Panah, B. Hazarika, P. Phukon, Prog. Theor. Exp. Phys. 2024 (2024) 083E02.
[200] C. Fairoos, T. Sharqui, Internat. J. Modern Phys. A 38 (2023) 2350133.
[201] S.-W. Wei, Y.-X. Liu, R.B. Mann, Phys. Rev. Lett. 129 (2022) 191101.